Check for updates

Boosting peroxymonosulfate activation by a novel bifunctional core-shell nanoreactor MnFe$_2$O$_4$@HZO for nitrilotris-methylenephosphonic acid removal

Shunlong Pan [a,*], Xinrui Guo [a], Xing Lu [a], Rong Li [a], Hao Hu [a], Xi Nie [a], Biming Liu [a,*], Rong Chen [b], Mingxin Zhu [a], Shengqiang Hei [c], Xianzheng Zhu [c], Shuo Zhang [d], Hua Zhou [a]

[a] School of Environmental Science and Engineering, Nanjing Tech University, Nanjing 210009, China
[b] Zhejiang Key Laboratory of Drinking Water Safety and Distribution Technology, College of Civil Engineering and Architecture, Zhejiang University, Hangzhou 310058, China
[c] State Key Joint Laboratory of Environment Simulation and Pollution Control, School of Environment, Tsinghua University, Beijing 100084, China
[d] Biological and Environmental Science and Engineering Division, King Abdullah University of Science and Technology (KAUST), Thuwal 23955-6900, Kingdom of Saudi Arabia

ARTICLE INFO

ABSTRACT

Advanced oxidation processes (AOPs) struggle to entirely remove phosphonates from wastewater, and the remaining phosphates easily cause secondary pollution. With MnFe$_2$O$_4$ as the core and hydrated zirconium oxide (HZO) as the shell, the magnetic core-shell nanoreactor MnFe$_2$O$_4$ @HZO with dual functions of "catalysis and adsorption" was designed to activate peroxymonosulfate (PMS) for nitrilotris-methylenephosphonic acid (NTMP) removal. Total phosphorus removal reached 96.5% within 180 min, with only 0.18 mg/L of phosphates left because of the full exploitation of active sites and adsorption sites. This is because of the strong inner-sphere complexation of shell for phosphates adsorption and the excellent electron transfer performance of the core for PMS activation. High NTMP removal under the protection of HZO shell could be obtained over wide pH (3−8) or complex water matrices. After five cycles, Mn leaching amount was only 0.4 mg/L. The study provides information on the design of core-shell catalysts in the PMS-AOP field for the comprehensive removal of contaminants.

1. Introduction

In industrial circulating cooling water (ICCW) systems, phosphonates are a significant class of synthetic complexing agents, which are widely used in scale and corrosion inhibition. Nitrilotris-methylenephosphonic acid (NTMP) is currently the most common scale inhibitor [1]. Phosphonates levels in ICCW drainage could reach 1.5–20 mg/L, and phosphonates with the concentrations of 0.088–7200 μg/L were detected in the river and the influent of municipal wastewater treatment plants (WWTPs) [2]. The risk of water eutrophication increased as a result of the photodegradation of phosphonates, which could produce bioavailable phosphates [3]. Among the traditional treatment methods, biodegradation technology was relatively inefficient and possessed overlong operation time [4], and the adsorption method [1] and flocculation precipitation method [5] could not degrade and

mineralize them, and were prone to producing secondary pollution. Therefore, it is necessary to develop efficient technologies to achieve the advanced removal of NTMP from ICCW.

Peroxymonosulfate (PMS)-based advanced oxidation process (PMS-AOP) has attracted interest because of its ability to replace hydroxyl radicals (•OH)-based AOP, which can generate excess reactive oxidative species (ROS), such as sulfate radicals (SO$_4^{\bullet-}$) and •OH, etc [6]. A common heterogeneous catalyst for PMS activation was Fe$_2$O$_3$ (mainly Fe(III)-oxide) [7]. In the system, Fe(III)-oxide must be firstly reduced to Fe(II)-oxide ($E^{\theta}_{Fe^{3+}/Fe^{2+}} = -0.77$ V vs. NHE), which inhibited the activation of PMS [8]. Therefore, Fe(II) regeneration was the critical rate-limiting step, requiring efficient electron transfer to enhance the reactivity of Fe$_2$O$_3$ [9]. A quick and efficient fix for this is to combine with other transition metals (such as Co, Cu, and Mn) to form bimetallic oxides [9]. Notably, MnO$_x$/Mn(II)-oxide (0.15 V) exhibited higher redox potential

than that of FeO_x/Fe(II)-oxide, with MnO_x having a stronger electron-donating ability due to Fe(II)-oxide regeneration [10]. Moreover, the synergistic effect made bimetallic oxide superior to monometallic oxide in activating PMS. Mn(II) was more environmentally friendly than Co(II) and Cu(II) with a lower negative impact on the environment [11]. However, strongly magnetic $MnFe_2O_4$ particles tended to agglomerate, resulting in poor dispersion and low activation efficiency [12]. It is also worth noting that researchers neglected the handling of produced phosphates throughout the degradation process in favor of improving the catalytic efficiency to achieve the efficient degradation of phosphonates in PMS system. More importantly, the phosphates that remained could cause the secondary pollution of water body, which needed to be adequately removed [11,13].

As the adsorbent, nano-metal (La, Al, Fe, Mn, Ti and Zr, etc.) oxide/hydroxide could effectively remove phosphates from the aqueous solution [14]. Hydrated zirconium (Zr) oxide (HZO) with large numbers of hydroxyl groups had higher specific surface area and active sites amongst them, particularly adsorbed phosphates through inner-sphere coordination [15]. Although the regeneration could be achieved by alkali desorption, HZO particles were tiny, easy to agglomerate, and difficult to recover [16].

Core-shell structure is a nano-scale ordered assembly material (core@shell) made of nanomaterial as the shell and coated with magnetic material at the core through chemical bonds or other forces [17]. The easy separation, recovery, and recycling of nanoreactors can be facilitated by the introduction of magnetic materials with magnetic response qualities into the core-shell structure [18]. The development of various magnetic core-shell materials as effective adsorbents or heterogeneous catalysts for AOPs to remove pollutants from water is now underway. On one hand, self-supporting magnetic nanoparticles as an adsorbent can be created by uniformly coating the nanomaterial on the surface of the magnetic nano-adsorbent (magnetic core@nano-adsorbent) [19]. This method addresses the shortcomings of the conventional fabrication method of magnetic adsorbent, which involves blocking the adsorption sites or pores on the surface of nano-absorbents with supported magnetic particles. To deposit $mZrO_2$ on the surface of Fe_3O_4 @SiO_2, Sarkar et al. [20] adopted the chemical precipitation method. The resulting Fe_3O_4 @SiO_2 @$mZrO_2$ had a larger specific surface area (107 m^2/g) and strong magnetic response with the adsorption capacity of 39.1 mg P/g. Additionally, n-butanol zirconium was uniformly coated on the surface of Fe_3O_4 microspheres using the sol-gel method to form Fe_3O_4 @ZrO_2 with a specific surface area of 135.8 ± 1.4 m^2/g. This material is easy to recycle and reuse, with the phosphorus removal process not hampered by external environment. Nevertheless, in the above studies, the Fe_3O_4 core only served as a magnetic response medium.

The core-shell structure, on the other hand, acts as a catalyst by preventing the magnetic catalytic core from aggregating and being disrupted by the surrounding solution environment. Moreover, the porosity of the shell can guarantee the diffusion of reactants and products, giving it a special advantage in PMS-AOP applications. Zeng et al. [21] recently developed a magnetic Fe/Fe_3C magnetic core with extensive dispersity, and the active sites were completely exposed thanks to the nitrogen-doped porous carbon shell, thereby exhibiting excellent catalytic performance. Zhang et al. [19] prepared a CoN/N-C@SiO_2 magnetic nanoreactor by nitridation using ZIF-67 @SiO_2 as a precursor, that could efficiently degrade tetracycline in PMS system. Similar to the above studies, the majority of researches used the shells of core-shell materials to adsorb and enrich the original contaminants, making it easier to get closer to the catalytic sites and increasing the catalytic efficiency. The "adsorption-catalysis" was the main process at the interface. Nevertheless, to accomplish the advanced treatment, the resulting phosphates by the catalytic oxidative degradation of phosphonates needed to be removed. Therefore, the adsorption and catalytic properties of magnetic core-shell materials must be further integrated.

To integrate advanced removal of NTMP from ICCW in PMS system,

we designed a bifunctional core-shell $MnFe_2O_4$ @HZO nanoreactor ($MnFe_2O_4$ as the core, HZO as the shell) with magnetic response, catalysis and adsorption. The NTMP removal efficiencies in different reaction processes were compared to confirm the availability of $MnFe_2O_4$ @HZO/PMS system. Subsequently, the activation mechanism and potential ROS in this system were emphatically analyzed and discussed. The intrinsic mechanisms of $MnFe_2O_4$ @HZO for PMS activation were further elaborated by density functional theory (DFT) calculations. In addition, the effects of several factors (initial pH, material dose, PMS and NTMP concentration, and water matrix) on the phosphates and total phosphorus (TP) removal efficiencies were examined. Besides, the reusability and stability of the catalyst by five cycles were evaluated for NTMP removal efficiency. Finally, detailed toxicity analysis of NTMP and potential degradation pathways were proposed. By establishing of bifunctional core-shell structure, our work was able to provide valuable insights for the comprehensive removal of pollutants.

2. Materials and methods

2.1. Materials

NTMP (>97%), 2-phosphonobutane-1,2,4-tricarboxylic acid (PBTC), hydroxyethyl diphosphonic acid (HEDP), ethylenediamine tetra(methylene phosphonic acid) (EDTMP), PMS and n-butanol zirconium (80 wt % in 1-butanol) were provided by Shanghai Aladdin Biochemical Co., Ltd. (China). Ethanol (EtOH), HNO_3, $NaNO_3$, ethylene glycol, polyethylene glycol and tert-butyl-alcohol (TBA) were purchased from Sinopharm Group (China). Cetyltrimethyl ammonium bromide (CTAB) and $NaHCO_3$ were purchased from Shanghai Lingfeng Chemical Reagent Co., Ltd. (China). NaCl, Na_2SO_4, K_2HPO_4, $FeCl_3$, $MnCl_2 \bullet 4H_2O$, sodium acetate (NaAc) and NaOH were prepared by Xilong Scientific Reagent Co., Ltd. (China). Iminodiphosphonic acid (IDMP) was purchased from American Sigma-Aldrich Chemical Reagent Co., Ltd. NaN_3, p-benzoquinone (p-BQ), (aminomethyl) phosphonic acid (AMPA), 5,5-Dimethyl-1-pyrroline N-oxide (DMPO), 2,2,6,6-tetramethylpiperidine (TEMP) and Fluorene methoxycarbonyl chloride (Fmoc-Cl) were purchased from Shanghai Macklin Biochemical Co., Ltd. The chemical reagents used were all analytical pure, and all solutions were prepared with deionized water.

2.2. Fabrication of $MnFe_2O_4$@HZO and characterization

As shown in Text S1, the sol-gel method was used to prepare a new magnetic core-shell nanocomposite catalyst ($MnFe_2O_4$ @HZO). Additionally, Scheme 1 shows a detailed illustration of the fabrication routes of $MnFe_2O_4$ and $MnFe_2O_4$ @HZO.

The surface morphology of materials was analyzed using scanning electron microscope (SEM, HITACHI S4800, Japan), and transmission electron microscopy (TEM, JEM 2100 F, JEOL, Japan) was used to further determine the internal structure and element distribution of $MnFe_2O_4$ @HZO. To measure the elemental composition of catalysts, an inductively coupled plasma emission spectrometer (ICP-OES, iCAP PRO, Thermo Fisher, US) was used. Thermogravimetric (TG, TGA5500, TA, US) was used to determine the chemical composition of $MnFe_2O_4$ @HZO at a heating rate of 10 °C/min. Through X-ray diffraction (XRD, Ultima IV, Rigaku, Japan) with $Cu_{K\alpha}$ radiation ($\lambda = 1.5406$ Å), the crystal crystalline phases of catalyst were determined. And the crystallite size was calculated using the Debye-Scherrer equation (Text S2). N_2 adsorption/desorption analyzer (APSP 2460, Micromeritics, US) was used to determine the specific surface area, pore size and pore volume distribution of materials. Then the specific surface area was calculated by Brunauer-Emmett-Teller (BET) method, while the pore size and pore volume were calculated by Barret-Joyner-Halenda (BJH) method. The hydrophilic and hydrophobic properties of materials were assessed by contact angle measuring instrument (JY-82B, Kruss DSA, Germany). The valence distribution of surface elements was detected using X-ray
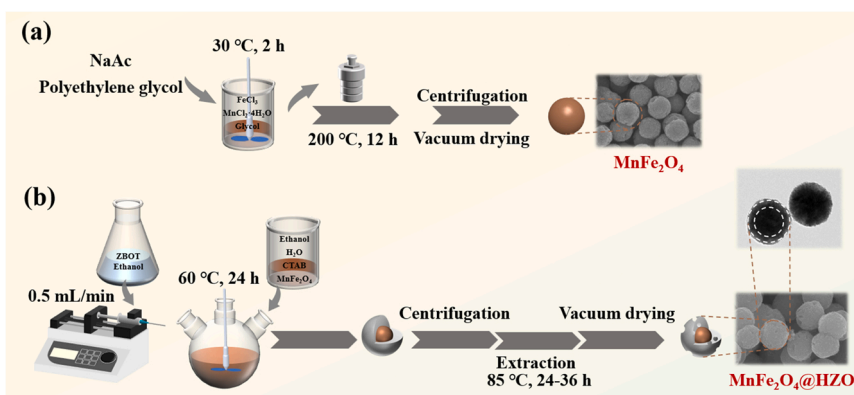
Scheme 1. Schematic illustration of the fabrication routes of (a) MnFe$_2$O$_4$ and (b) MnFe$_2$O$_4$@HZO.

photoelectron spectroscopy (XPS, K-Alpha, Thermo Scientific, US). The vibrational and structural properties of nanomaterials were evaluated using the Raman spectrum (Renishaw invia reflex, England). The zeta potential of materials was ascertained using zeta potential analyzer (ZetaPALS, Brookhanven Instruments, US). A vibration magnetometer (VSM, LakeShore7404, US) was employed in testing the hysteresis loop of catalysts. Electrochemical measurements were performed on an electrochemical workstation (CHI760E, CH, Instruments Inc., China) (the detailed information in Text S3).

2.3. Experiments

All NTMP removal tests were conducted in a thermostatic water-bath shaker (THZ-82, Shanghai Yuming, China), and NTMP concentrations selected were consistent with the actual levels of ICCW. Typically, a preset amount of PMS was mixed with NTMP (0.05–0.3 mM, 4.65–27.9 mg P/L) in a conical flask and diluted to 50 mL. pH$_0$ was then adjusted with 0.1 M HNO$_3$ and 0.1 M NaOH, before catalysts (0.2–1.0 g/L) were added to the mixed solution with ultrasonic for 5 min. Finally, the conical flask was then shaken at 35 °C and 200 rpm for 3 h. To determine the concentrations of PO$_4^{3-}$ and TP in the filtrate, 2.0 mL sample was taken at the given time intervals, and then filtered with a 0.22 μm filter membrane. The pseudo-first-order kinetic equation was used to calculate the relevant degradation efficiency constant (k_{obs}) [22]. The effects of the different concentrations of anions (Cl$^-$, NO$_3^-$, SO$_4^{2-}$ and HCO$_3^-$) and humic acid (HA) for NTMP removal were evaluated. The simulated ICCW was prepared with a molar ratio of CaCl$_2$ and NaHCO$_3$ of 1:2 at a hardness of 320 mg/L (calculated as CaCO$_3$) and pH 8.2. In the cycling experiments, the exhausted MnFe$_2$O$_4$@HZO was collected by magnetism, and washed with 1 M NaOH and distilled water successively, before drying in an oven at 70 °C for the next cycle.

2.4. Analytical methods

Ammonium molybdate spectrophotometry was adopted to determine PO$_4^{3-}$ and TP concentrations. To calculate their removal efficiencies, and the detailed description of calculation was provided in Text S4 [1]. It is worth noting that the samples should be digested with persulfate prior to assessing the TP concentration by using a UV-Vis spectrophotometer (UV-1900PC, AOE, China). A pH meter (pH FE28, METTLER TOLEDO, Switzerland) was used to determine the solution pH. Electron paramagnetic resonance (EPR, A300, Bruker, Germany) was used to detect ROS, and 0.1 M DMPO or 50 mM TEMP was added to the samples (1 mL) before assay. High-performance liquid chromatography (HPLC, LC-20A, Shimadzu, Japan) was utilized to determine IDMP and AMPA. Liquid chromatography-mass spectrometers (LC-MS, Vanquish/QE-HFX, ThermoFisher, US) were used in the investigation of intermediates. The concentrations of NH$_3$-N and NO$_2^-$-N were detected by UV-Vis multi-parameter water quality tester (LH-3BA, Lianhua,

China), while the ion chromatography (IC, ICS-600, Thermo Scientific, US) with an eluent (4.5 mM Na$_2$CO$_3$ and 0.8 mM NaHCO$_3$)was used for the determination of NO$_3^-$-N and formic acid (HCOOH). A total organic carbon analyzer (TOC, TOC-VCPH, Shimadzu, Japan) was used in measuring the concentration of organic carbon in the solution.

2.5. Computational details

DFT calculations are provided in Text S5.

3. Results and discussion

3.1. Design and structural characterizations of MnFe$_2$O$_4$@HZO

Fig. 1 shows SEM and TEM images of catalysts. MnFe$_2$O$_4$ is a sphere with an average diameter of ~290 nm (Fig. 1(a)), while the average diameter of HZO is only ~200 nm (Fig. 1(b)). The surface of MnFe$_2$O$_4$ spheres is uniformly coated with HZO particles, increasing the diameter of the obtained catalyst to ~320 nm (Fig. 1(c)). The core-shell structure of MnFe$_2$O$_4$@HZO spheres is produced as new HZO layers generate on the surface of MnFe$_2$O$_4$ spheres. Additionally, the non-magnetic HZO shells make the resulting spheres dispersed evenly without distinct agglomeration from the TEM image (Fig. 1(d)), resulting in MnFe$_2$O$_4$@HZO particles with greater specific surface area.

HRTEM analyses were performed to deeply understand the obtained morphology of MnFe$_2$O$_4$@HZO nanocomposite. The HRTEM image of MnFe$_2$O$_4$@HZO (Fig. 1(e)) clearly shows the lattice fringes of MnFe$_2$O$_4$ (d=0.297, 0.253 and 0.148 nm), consistent with the crystallites at (220), (311) and (440), respectively [23]. The predominant elements of Fe, Mn, O and Zr are uniformly distributed in the MnFe$_2$O$_4$@HZO sphere, and Zr maybe evenly distribute around the core in the form of Zr-O and Zr-Zr bonds (Fig. 1(f-i)). To maximize the use of metal atoms, optimal catalysts and adsorbents contain active redox sites and adsorption sites, that are uniform and dispersed [13]. The proportions of Fe, Mn and Zr were determined via ICP-OES analysis to be 80%, 8% and 12%, respectively (Table S1), further proving that HZO was successfully coated on the surface of MnFe$_2$O$_4$.

N$_2$ adsorption/desorption curves of MnFe$_2$O$_4$@HZO, MnFe$_2$O$_4$ and HZO are all type IV curves (Fig. 2(a)), and the pore diameters are 4.85, 4.35 and 23.9 nm, respectively based on the classification of the International Union of Pure and Applied Chemistry (IUPAC) (Table S2). When P/P$_0$ is in the range of 0.2–1.0, a hysteresis loop similar to H$_3$ type can be observed. This further proves that the magnetic MnFe$_2$O$_4$@HZO is mesoporous material with a narrow pore size distribution [24]. Additionally, the inner and outer double-layer surface of the core-shell structure provides MnFe$_2$O$_4$@HZO a higher specific surface area (170 m^2/g) than that of MnFe$_2$O$_4$ (70 m^2/g) and HZO (81 m^2/g), because makes it have higher specific surface area. The relevant TG curves were analyzed to understand the structure and performance of
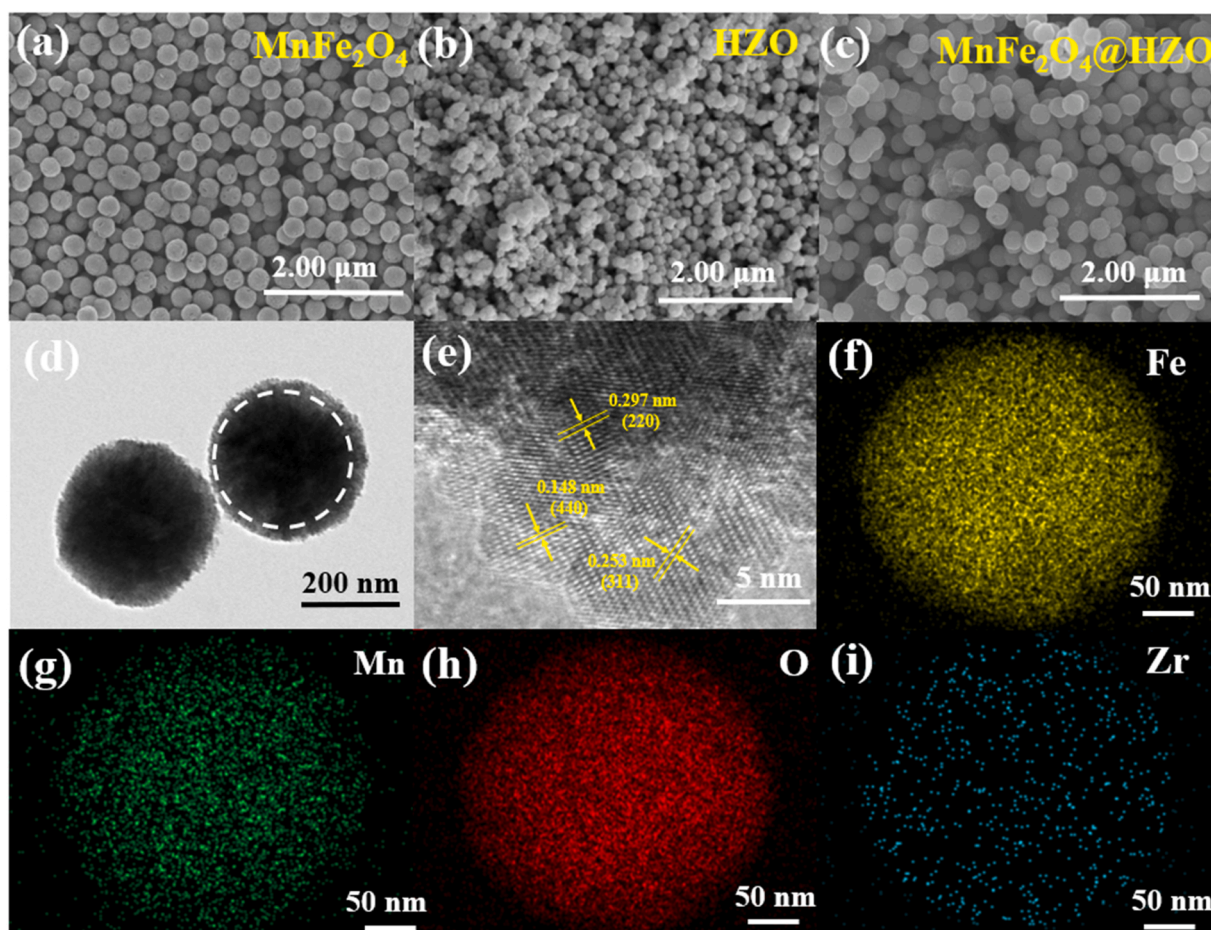
Fig. 1. SEM images of (a) MnFe$_2$O$_4$, (b) HZO and (c) MnFe$_2$O$_4$@HZO. (d) TEM and (e) HRTEM images of MnFe$_2$O$_4$@HZO with the elemental mapping (f-i) images.

catalyst (Fig. 2(b)). When the temperature gradually increases to 400 °C, the weight loss of MnFe$_2$O$_4$ @HZO and MnFe$_2$O$_4$ is 11.2% and 9.8%, respectively. It's hypothesized that the difference in weight is the loss of adsorbed water on the surface of HZO shell (25–200 °C) and the removal of partial bound water and few hydroxyl groups. Subsequently, as the temperature increases to 1000 °C, TG curves begin to flatten out and the weight loss of MnFe$_2$O$_4$ @HZO and MnFe$_2$O$_4$ is only 4.3% and 4.2%, due to the dehydrogenation and dehydroxylation [25]. It's observed that core-shell MnFe$_2$O$_4$ @HZO exhibits great thermal stability.

XPS survey spectrum confirms the presence of Fe, Mn, O and Zr in MnFe$_2$O$_4$ @HZO (Fig. S1). Spin-orbit doublets of Mn 2p$_{1/2}$ and Mn 2p$_{3/2}$ constitute the Mn 2p, while Mn(II) (641.0 eV) and Mn(III) (644.9 eV) exist in the deconvolution of Mn 2p$_{3/2}$ [26] (Fig. 2(c)). The characteristic peaks of Fe 2p binding energy at 710.2, 712.2, 718.1 and 725.3 eV correspond to Fe(II) 2p$_{3/2}$, Fe(III) 2p$_{3/2}$, Fe(II) 2p$_{1/2}$ and Fe(III) 2p$_{1/2}$ (Fig. 2(d)) [27]. Metal oxides (M-O, 529.8 eV), metal surface hydroxyl groups (M-OH, 531.4 eV) and adsorbed water (H$_2$O, 533.8 eV) are the three main components of O 1 s, where M-OH content (60.15%) is the highest in the total oxygen (Fig. 2(e)), which is much higher than that of Fe$_3$O$_4$ (25.37%) reported in the literature [28]. This demonstrated how the addition of partial Fe by Mn and Zr boosted the M-OH species in the structure, which was closely related to the improvement of adsorption capacity. Additionally, Zr 3d can be fitted to three peaks, where two peaks at 182.5 and 184.6 eV belong to Zr-O, and the peak at 186.2 eV assigns to Zr-Zr [29] (Fig. 2(f)). Consequently, HZO exists in the form of Zr-O/Zr-Zr, and the Zr-OH of HZO enhances the M-OH on the surface of MnFe$_2$O$_4$ @HZO.

XRD pattern demonstrates that HZO is amorphous in its as-prepared because there is no obvious diffraction peak in HZO (Fig. 2(g)).

Diffraction peaks of MnFe$_2$O$_4$ are well indexed to the crystal planes of the standard of magnetite (JCPDS No. 19–0629), demonstrating that MnFe$_2$O$_4$ had higher crystallinity [30]. According to the Debye-Scherrer equation (Eq. (S1)), the average crystallite sizes of MnFe$_2$O$_4$ and MnFe$_2$O$_4$ @HZO are 15.0 and 10.6 nm, respectively. This could be attributed to the cover of HZO which inhibited the growth of MnFe$_2$O$_4$ crystals, resulting in relatively low crystallite size [23,31]. Subsequently, Raman spectrum is shown in Fig. S2, with the probed peaks between 100 and 1000 cm^{-1} belonging to the vibrations of MnFe$_2$O$_4$ [23]. A$_{1 g}$ and E$_g$ models belong to tetrahedron (a site) and octahedron (b site), respectively [32]. The symmetric stretching of O atom along the M^{n+}-O bond is associated with the A$_{1 g}$ model observed at 600–690 cm^{-1}, and asymmetric bending of the M^{n+} by the O atom is associated with the E$_g$ model at 300–350 cm^{-1} [33]. Moreover, T$_{2 g}$ model displays a weaker peak band at 197–220 cm^{-1}, corresponding to the translational motion of the entire Mn$^+$O$_4$ [32]. However, the Raman spectrum of MnFe$_2$O$_4$ @HZO does not differ significantly compared with MnFe$_2$O$_4$, indicating that there was no phase transition. However, there is a significant increase in the peak intensities at 300–350 and 600–690 cm^{-1}, which maybe due to the bonding of electrostatic interaction between MnFe$_2$O$_4$ and HZO. It proved that HZO was successfully covered on the MnFe$_2$O$_4$ core. And this phenomenon is consistent with the results obtained by XRD.

A vital tool for obtaining material magnetic susceptibility and its hysteresis loop is VSM technology. The Magnetization saturation (Ms) value of HZO is zero (Fig. 2(h)). This confirms the superparamagnetic properties of MnFe$_2$O$_4$ (64.2 emu/g) and MnFe$_2$O$_4$ @HZO (49.7 emu/g) at room temperature since the hysteresis loops pass through the origin and have a typical S-shape, and both show negligible remanence (Mr)
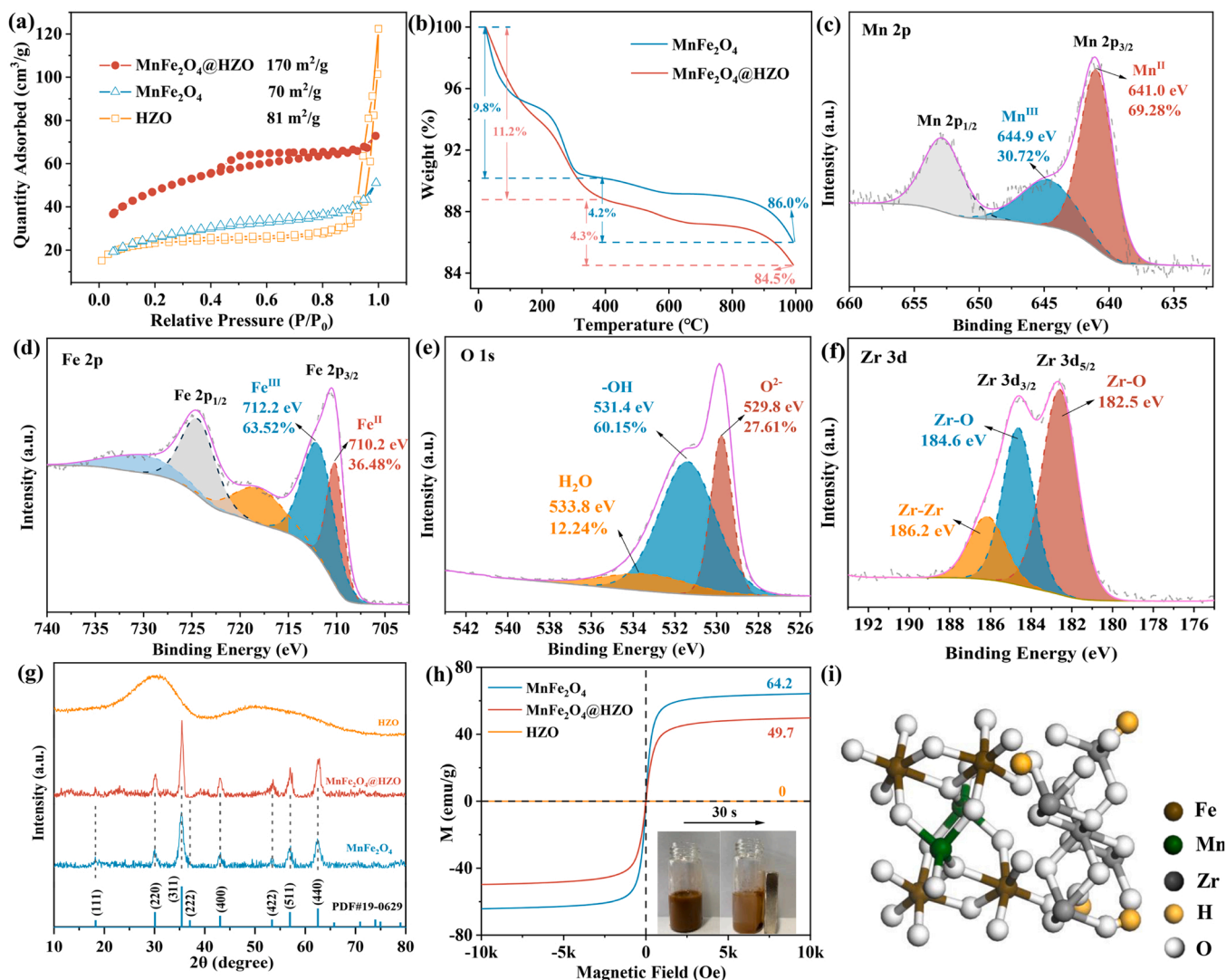
Fig. 2. (a) N$_2$ adsorption/desorption isotherms and (b) TG analysis of catalysts. (c) Mn 2p, (d) Fe 2p, (e) O 1s and (f) Zr 3d XPS spectra of MnFe$_2$O$_4$@HZO. (g) XRD patterns and (h) Magnetic hysteresis loops of catalysts. (i) Molecular structure of MnFe$_2$O$_4$@HZO.

and coercivity (Hc). Furthermore, the Ms value of MnFe$_2$O$_4$@HZO was significantly reduced by the presence of nonmagnetic HZO shell, yet the catalyst could still be easily separated from the solution by magnet within 30 s. Thus, to remove contaminants from an aqueous solution and avoid secondary pollution, MnFe$_2$O$_4$@HZO can be used as a recyclable magnetic catalyst. Based on the above characterization results,
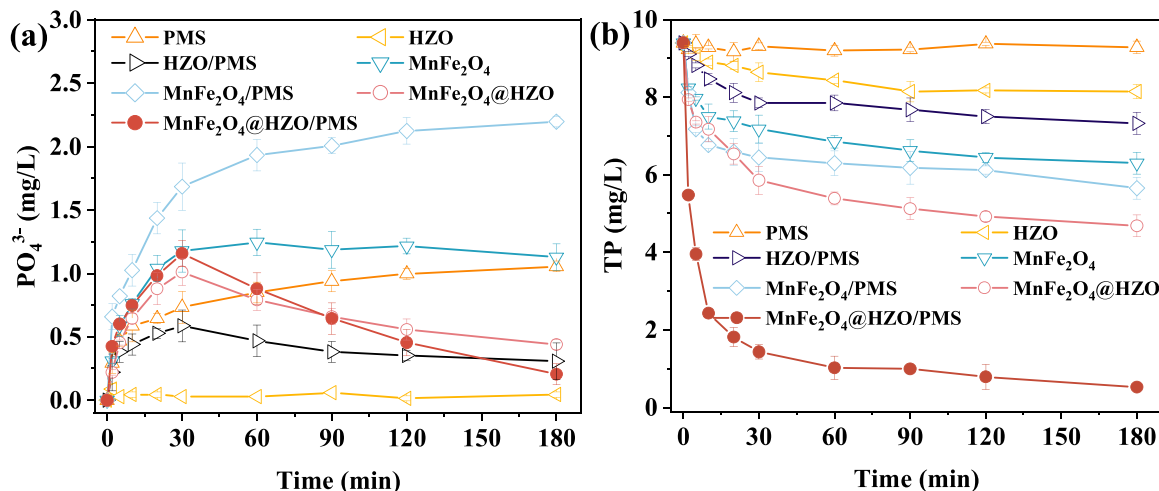
Fig. 3. Effect of different systems on NTMP removal. (35 °C, pH$_0$ 7, [NTMP]$_0$ = 0.1 mM (9.3 mg TP/L), [PMS]$_0$ = 1.5 mM, material dose = 0.5 g/L).

the MnFe$_2$O$_4$ @HZO structural model was constructed (Fig. 2(i)). In the interior of Fe-Mn spinel, there are two sub-lattices (a-site for tetrahedron and b-site for octahedron) in which Fe and Mn atoms are uniformly distributed in a-site and b-site. Accordingly, HZO is electrostatically bound to MnFe$_2$O$_4$, simultaneously introducing excess -OH on the surface of MnFe$_2$O$_4$ @HZO.

### 3.2. Comparison of different reaction processes

Various processes were used to compare the effectiveness of removing TP and phosphorus. After 180 min in the presence of PMS alone, just a small amount of phosphates (1 mg/L) are generated indicating that PMS alone had a poor oxidation effect on NTMP (Fig. 3(a)). It is possible that partial NTMP was adsorbed rather than decomposed by HZO, because HZO particles only reduced TP concentration to 8.15 mg/L without producing phosphates (Fig. 3(b)). However, TP removal efficiency is slightly higher than that of HZO, and the phosphates concentration of HZO/PMS system is always lower than that of PMS alone within 180 min. This maybe the case because phosphates generated from NTMP decomposition by PMS could be continuously adsorbed by HZO.

It is interesting to note that after 180 min, phosphates concentration reaches 1.22 mg/L in the presence of MnFe$_2$O$_4$ alone. On one hand, MnFe$_2$O$_4$ could capture NTMP and form a complex, and on the other hand, it could also degrade a small quantity of NTMP into phosphates by MnFe$_2$O$_4$ through internal-electron-transfer autocatalytic oxidation [34]. In this procedure, the dissolved oxygen (DO) would be released to the Mn(II)-oxides in the nodules, which were further oxidized to form Mn(IV)-oxides or transient Mn(III)-intermediates [35]. Then, we detected that DO concentration in the system decreased from initial 4.4 mg/L to 3.4 mg/L. Worth noting, we will continue with the research on the autocatalytic oxidation of MnFe$_2$O$_4$ in the future, which will not affect the conclusion of this study. Phosphates and TP concentrations appear to be lower in the MnFe$_2$O$_4$ @HZO system compared to MnFe$_2$O$_4$, indicating that HZO shell absorbed the declining phosphates.

NTMP removal by MnFe$_2$O$_4$/PMS and MnFe$_2$O$_4$ @HZO/PMS systems was emphatically compared. Phosphate concentration in MnFe$_2$O$_4$/PMS system (2.27 mg/L) is higher than that in MnFe$_2$O$_4$ @HZO/PMS system, further demonstrating that HZO shell had superior phosphates adsorption capacity. In addition, TP removal efficiencies of MnFe$_2$O$_4$/PMS (k_{obs}=0.028 min^{-1}) and MnFe$_2$O$_4$ @HZO/PMS systems (0.094 min^{-1}) are 39.8% and 94.1%, respectively within 180 min (Fig. S3). In this instance, these two systems simultaneously absorbed and broke down the NTMP as phosphates were produced, with the MnFe$_2$O$_4$ @HZO/PMS system showing higher degradation rate and efficiency for NTMP. It is also worth noting that phosphates concentration emerges at the peak inflection point at 30 min in HZO/PMS, MnFe$_2$O$_4$ @HZO and MnFe$_2$O$_4$ @HZO/PMS systems. The inflection point was caused by the failure of HZO to timely adsorb the emerging phosphates in solution since the adsorption rate was lower than NTMP degradation rate [36]. After 30 min, phosphates concentration gradually decreases to a certain value with the slow adsorption of emerging phosphates on the HZO shell. Notably, the pH values of solutions in the MnFe$_2$O$_4$/PMS and MnFe$_2$O$_4$ @HZO/PMS systems both significantly drop to 3.67 and 3.47 after reaction, respectively (Table S4). On one hand, a lot of H$^+$ would be produced when the PMS was hydrolyzed, on the other hand, the electron transfer between the catalyst and PMS led to a decrease in solution pH (Eqs. (1) and (2)). Besides, NTMP degradation efficiency in the MnFe$_2$O$_4$ @HZO/PMS system is indeed higher than that of MnFe$_2$O$_4$ @HZO system, which produces a higher concentration of phosphates. pH variation of the MnFe$_2$O$_4$ @HZO system was slight. And the pH decrease of reaction system could promote the protonation of HZO surface and improved the adsorption capacity of phosphates. Thus, the concentrations of the remaining phosphates in the MnFe$_2$O$_4$ @HZO/PMS and MnFe$_2$O$_4$ @HZO systems are similar.

Several other processes have been reported for the removal of NTMP

(Table S5). In comparison, the k_{obs}-TP in this study is remarkably higher than that of UV/Persulfate process (0.018 min^{-1}) [37]and Fe(III)/UV/-NaOH process (0.032 min^{-1}) [1]. Although the homogeneous Co (II)/PMS system (0.150 min^{-1}) has a higher k_{obs}-NTMP, the phosphates generated during this reaction are prone to secondary contamination [38]. Especially, k_{obs}-TP of Fe-electrocoagulation (1.021 min^{-1}) and Al-electrocoagulation (0.917 min^{-1}) processes with strong performance is much higher than other AOPs, but unmineralized NTMP still has potential hazards [39]. In conclusion, the MnFe$_2$O$_4$ @HZO/PMS system employed an "adsorption-catalysis-adsorption" mechanism. Firstly, NTMP and PMS were attracted to the surface of MnFe$_2$O$_4$ @HZO. Then, the core of the material activated PMS to destroy NTMP by ROS, and the outside layer of material successfully attracted the generated phosphates. In this method, the catalytic effect was dominant and the MnFe$_2$O$_4$ core had greater adsorption effect on NTMP than the HZO shell. On the contrary, compared to NTMP, HZO shell had better adsorption effect on phosphates.

$$Fe^{3+} + HSO_5^- \rightarrow Fe^{2+} + SO_5^{\bullet-} + H^+ \quad (1)$$

$$Mn^{3+} + HSO_5^- \rightarrow Mn^{2+} + SO_5^{\bullet-} + H^+ \quad (2)$$
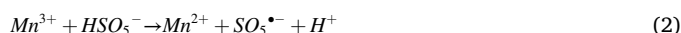
3.3. Activation mechanism and possible ROS

3.3.1. Activation mechanism of MnFe$_2$O$_4$@HZO/PMS system

Electrochemical analysis can be used to determine the function of electron transfer in the reaction system. Compared to the cyclic voltammetry (CV) curves of HZO and MnFe$_2$O$_4$, MnFe$_2$O$_4$ @HZO has higher current density and redox peaks at 0.7 V vs. Ag/AgCl (Fig. 4(a)). The electrochemical redox was significantly influenced by the MnFe$_2$O$_4$, which may be related to the redox electron transfer between Fe(II)/Fe (III) and Mn(II)/Mn(III) [40,41]. Additionally, their electrochemical impedance spectroscopy (EIS) characteristics were compared. The semicircle with a smaller diameter indicates a lower charge transfer impedance at the electrode-electrolyte interface in Nyquist plots, where high frequency and low frequency correspond to electron transfer and mass diffusion, respectively [42]. In comparison, MnFe$_2$O$_4$ @HZO particles have a smaller semicircular diameter in the high-frequency region (Fig. 4(b)), showing HZO shell improved the charge transfer and conductivity of MnFe$_2$O$_4$ core, thus making the electron transfer easier on the MnFe$_2$O$_4$ @HZO electrode. The larger current signals in the linear sweep voltammetry (LSV) curves are then produced by MnFe$_2$O$_4$ @HZO/PMS and MnFe$_2$O$_4$ @HZO/PMS/NTMP systems (Fig. 4(c)). Immediately, after the addition of PMS (1.5 mM) and NX (0.1 mM) at 90 s and 270 s, respectively, robust current fluctuations can be observed. Similarly, MnFe$_2$O$_4$ @HZO/PMS system generates a larger current than MnFe$_2$O$_4$/PMS system, once more indicating the greater ability to transfer charges and oxidize (Fig. 4(d)). Because HZO shell had strong adsorption affinity for HSO$_5^-$, thus promoting the activation of PMS [43].
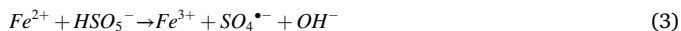
XPS was performed on the exhausted catalyst to elucidate the chemical state variation of Fe and Mn and provided us with a possible catalytic pathway for MnFe$_2$O$_4$ @HZO/PMS system. Mn(II) relative content at 641.0 eV improves from 69.28% to 71.82% after reaction, and Mn(III) at 644.9 eV drops from 30.72% to 28.18% (Figs. 2(c) and 4 (e)). About 2.54% Mn(III) is converted into Mn(II), illustrating that the remaining HSO$_5^-$ in the system reduced Mn(III) to Mn(II). Besides, Mn (II) and NTMP readily formed Mn(II)-NTMP-complexes, which were subsequently transformed into Mn(III)-NTMP due to molecular oxygenation and catalytic oxidation, but finally the cleavage of the C-P bond triggered by internal electron transfer led to the reduction of Mn (III) to Mn(II) [34]. Fig. 4(f) displays the XPS analysis results of Fe, which revealed that Fe(II) and Fe(III) components change from 36.48%, 63.52–43.60% and 56.40%, respectively, and about 7.12% of Fe(III) species turns to Fe(II). The relative content of Fe(II) after reaction seems to increase, probably because the standard redox potential of Fe(III)/Fe
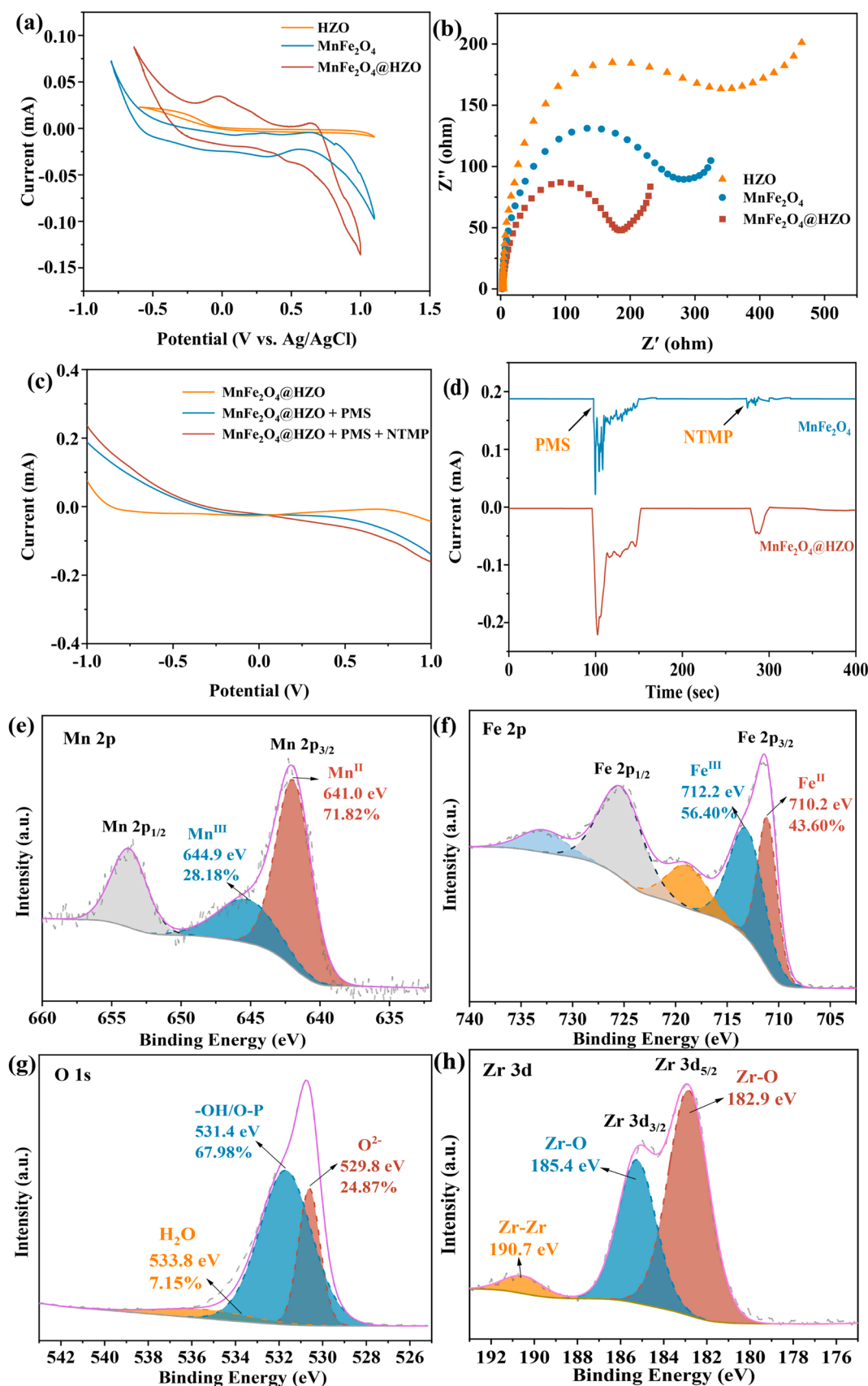
Fig. 4. (a) CV curves at a scan rate of 50 mV/s and (b) EIS Nyquist plots of different catalysts. (c) i-t curves and (d) LSV curves under different conditions. (pH_0 7, $[PMS]_0 = 1.5$ mM, $[NTMP]_0 = 0.1$ mM (9.3 mg TP/L)) (e) Mn 2p, (f) Fe 2p, (g) O 1s and (h) Zr 3d XPS spectra of MnFe$_2$O$_4$@HZO after reaction.

(II) (0.77 V) was higher than that of MnO/Mn_2O_3, and Mn(III) could reduce Fe(III) to Fe(II) (0.15 V), ensuring the continuous activation of PMS [44]. As a result, both Mn(II) and Fe(II) donated electrons to PMS, which triggered the decomposition of PMS to produce $SO_4^{\bullet-}$ (Eqs. (3) and (4)) [11]. Subsequently, high-valence Mn and Fe were reduced by HSO_5^- to complete the redox cycle (Eqs. (1) and (2)), facilitating the catalytic effect of $MnFe_2O_4$ [45].

$$Fe^{2+} + HSO_5^- \rightarrow Fe^{3+} + SO_4^{\bullet-} + OH^- \tag{3}$$

$$Mn^{2+} + HSO_5^- \rightarrow Mn^{3+} + SO_4^{\bullet-} + OH^- \tag{4}$$

We also investigated the adsorption mechanism of $MnFe_2O_4$ @HZO using XPS spectra, and the results of metal atomic ratio on the catalyst surface (Table S3) are highly consistent with ICP analysis. A new P element peak appeared at the binding energy of 134.1 eV (Fig. S4), and was uniformly distributed on the surface of exhausted $MnFe_2O_4$ @HZO from TEM mapping (Fig. S5). O 1 s spectrum was assigned to metal oxides (M-O), metal surface hydroxyl groups (M-OH) and adsorbed water (H_2O), with binding energies of 529.8, 531.4 and 533.8 eV, respectively (Fig. 4(g)) [28]. The content of M-O component at 529.8 eV dropped from 27.61% to 24.87% after phosphates adsorption, attributable to the formation of Zr-O-P bond [15]. Theoretically, phosphorus could lead to the reduction of M-OH species via formation of M-O/OH-P bonds [15]. Interestingly, the content of M-OH groups grew from 60.15% to 67.98% at 531.4 eV, likely due to strong spontaneous mutual complexation between M-OH sites and the target phosphates [46].

Core-level Zr 3d spectrum can be deconvoluted into three peaks, assigning to Zr-O (182.5 eV, 184.6 eV) and Zr-Zr (190.7 eV) [29] (Fig. 4 (h)). Zr-O and Zr-Zr bonds shift from 182.5 and 184.6 eV to 182.9 and 185.4 eV, respectively after phosphates adsorption. A Zr-O-P inner--sphere coordination structure formed between -Zr-OH and $H_2PO_4^-/HPO_4^{2-}$ accounts for these shifts [28,47]. Additionally, phosphate binding energy (133.8 eV) is analogous to that of $FePO_4 \bullet 2H_2O$ (133.6 eV), confirming the Fe-O-P bond formation in O 1 s spectrum [28]. Based on above analysis, $MnFe_2O_4$ @HZO could establish stable internal coordination complex with $H_2PO_4^-/HPO_4^{2-}$ mainly via -Zr-OH bonds (Eq. (5)) [47].

$$Zr-(OH)_y + bH_xPO_4^{(3-y)-}(aq) \rightarrow Zr-(OH)_{y-b}\left[H_xPO_4^{(3-x)-}\right]_b + bOH^-(aq) \tag{5}$$
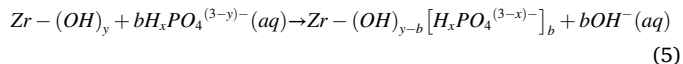
3.3.2. Determination of ROS and their contributions

Quenching experiment is an effective method to study the existence and contribution of ROS for NTMP degradation. TBA reacts rapidly with $\bullet OH$ ($k_1 = 3.8$–7.6×10^8 $M^{-1} \bullet s^{-1}$) but rather slowly with $SO_4^{\bullet-}$ ($k_2 = 4.0$–9.1×10^5 $M^{-1} \bullet s^{-1}$) [19]. Similarly, EtOH reacts rapidly with $\bullet OH$ ($k_3 = 9.1 \times 10^6$ $M^{-1} \bullet s^{-1}$) and $SO_4^{\bullet-}$ ($k_4 = 3.5 \times 10^7$ $M^{-1} \bullet s^{-1}$) [21]. Therefore, TBA and EtOH were selected as the quenchers of $\bullet OH$ and $SO_4^{\bullet-}$, respectively. TP removal efficiency drops to 78% when the ratio of TBA to PMS is 1200, and k_{obs} sits at 0.028 min^{-1} (Fig. 5(a)). After further increasing the addition of TBA concentration, TP removal efficiency stabilizes (Fig. S6(a)). TP removal efficiency drops to 55.1% (0.013 min^{-1}) at most when the ratio of EtOH to PMS reaches 1600 (Fig. S6(b)). Since excess TBA and EtOH don't completely inhibit NTMP degradation, $\bullet OH$ and $SO_4^{\bullet-}$ can both participate in the reaction, $SO_4^{\bullet-}$ playing an important role.

NaN_3 can effectively quench $^1O_2$ (2×10^9 $M^{-1} \bullet s^{-1}$), $\bullet OH$ (1.1×10^{10} $M^{-1} \bullet s^{-1}$) and $SO_4^{\bullet-}$ (2.5×10^9 $M^{-1} \bullet s^{-1}$) simultaneously. However, the
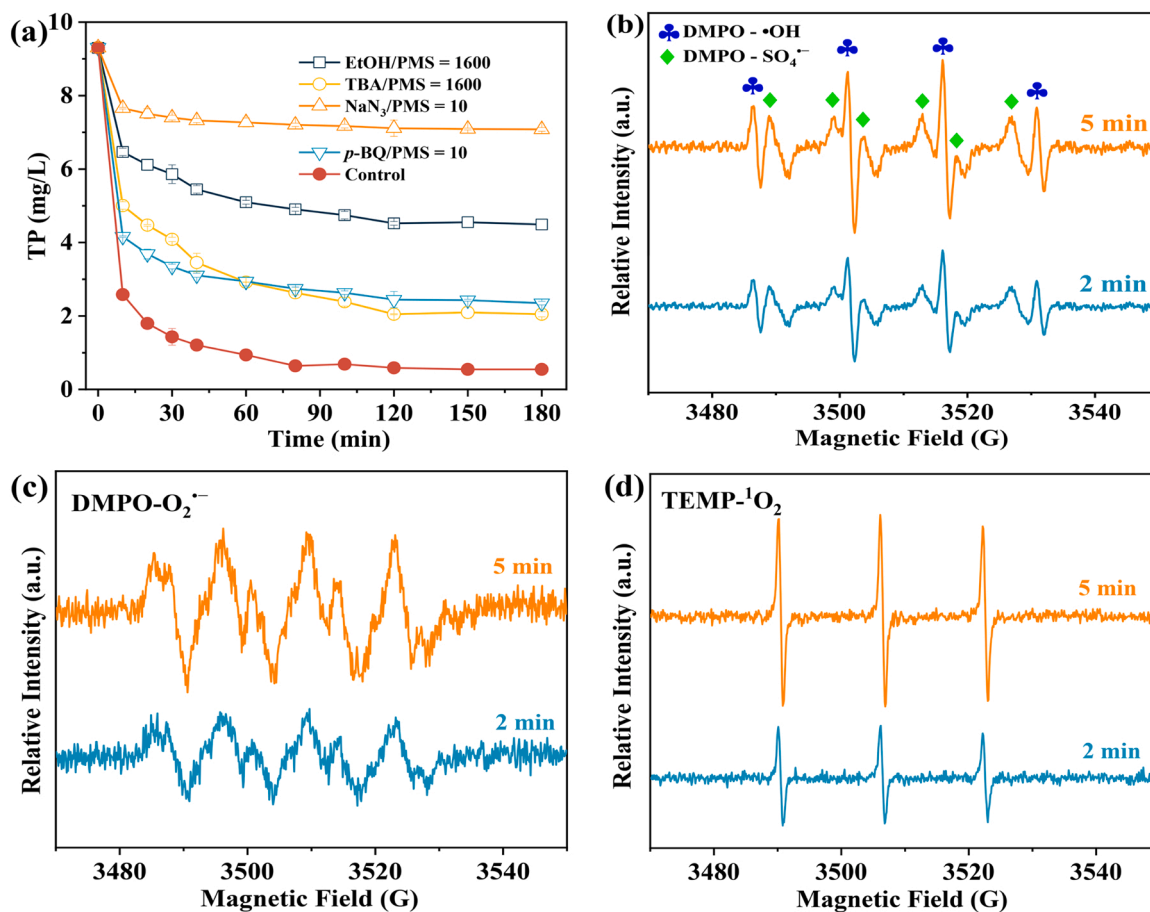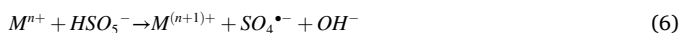

Fig. 5. (a) Effect of ROS scavengers on TP removal. (b-d) EPR spectra with the addition of DMPO and TEMP. (35 °C, pH_0 7, $[NTMP]_0 = 0.1$ mM (9.3 mg TP/L), $[PMS]_0 = 1.5$ mM, $MnFe_2O_4$@HZO = 0.5 g/L).

reaction between NaN₃ and PMS is slow relative to that between activator and PMS, thus NaN₃ was used as $^1O_2$ quencher [48]. TP removal efficiency declines rapidly to 43.3% (0.010 min^{-1}) and 23.9% (0.005 min^{-1}) when the addition concentration of NaN₃ is 2 times and 10 times than that of PMS, respectively (Fig. S6(c)). The quenching effect of NaN₃ is better than that of TBA and EtOH, showing $^1O_2$ is an important ROS for NTMP degradation. On the other hand, TP removal efficiency only decreases to 74.7% (0.036 min^{-1}) when high-concentration *p*-BQ (*p*-BQ/PMS=10) is utilized as a quencher for $O_2^{\bullet-}$ (9.6 ×10⁸ M^{-1}•s^{-1}) (Fig. S6(d)). This indicates that $O_2^{\bullet-}$ plays a restricted role for NTMP degradation. According to the results of quenching experiment, the contribution ratio of each ROS to NTMP degradation was calculated [49]. The contribution rates of •OH, $SO_4^{\bullet-}$, $^1O_2$ and $O_2^{\bullet-}$ are 19.3%, 42%, 31.2% and 7.5%, respectively (Table S6). It can thus be stated that the contributions of ROS follow in sequence: $SO_4^{\bullet-}>^1O_2 > \bullet OH>O_2^{\bullet-}$.

EPR was further employed to verify the presence of ROS. An EPR signal with the intensity ratio of 1:2:2:1 was observed, owing to the existence of DMPO-•OH ($\alpha_N = \alpha_H$=14.9 G) and the formation of •OH in the system [5] (Fig. 5(b)). The signal peaks of DMPO-$SO_4^{\bullet-}$ (α_N= 13.5 G, α_H= 10.0 G, α_H= 1.1 G, α_H= 0.6 G) were also observed around •OH signal, proving the existence of $SO_4^{\bullet-}$ [50]. Interestingly, a strong four-wire EPR characteristic signal of DMPO-$O_2^{\bullet-}$ was also detected [19] (Fig. 5(c)). The characteristic signal of 1:1:1 intensity of TEMP-$^1O_2$ adduct is distinct proof of $^1O_2$ formation [51] (Fig. 5(d)). It's observed that the detection results of EPR were highly consistent with ROS quenching experiments, and both radical ($SO_4^{\bullet-}$, •OH, $O_2^{\bullet-}$) and non-radical ($^1O_2$) contributed to NTMP degradation.

On basis of the above analysis, we proposed the mechanism and process of ROS generation. Firstly, MnFe₂O₄ @HZO facilitated the enrichment of NTMP, which enabled it to rapidly diffuse to the active site. The encapsulation and confinement effects of core-shell structure played a key role in improving the degradation efficiency and stability of the active site. Subsequently, the enriched NTMP can be confined in the microenvironment formed by core-shell structure, causing a higher instantaneous NTMP concentration in the void space. This provides the driving force for the enhanced degradation activity. The O-O bond in PMS was broken to generate $SO_4^{\bullet-}$ (Eq. (6)), which reacted with H₂O or OH⁻ to form •OH [11] (Eqs. (7) and (8)). MnFe₂O₄ core donated electrons to O₂ to generate $O_2^{\bullet-}$ [11,52] (Eq. (9)). •OH could generate $^1O_2$ through disproportionation [52] (Eq. (10)). The formation of $SO_5^{\bullet-}$ was dependent on the destruction of H-O bond in PMS, a pre-requisite to the reaction with H₂O that yields $^1O_2$ [53] (Eqs. (11) and (12)). Thus, the adsorbed NTMP molecules were attacked by the synergistic actions of radical and non-radical reaction.

$$M^{n+} + HSO_5^- \rightarrow M^{(n+1)+} + SO_4^{\bullet-} + OH^- \tag{6}$$

$$SO_4^{\bullet-} + H_2O \rightarrow SO_4^{2-} + \bullet OH + H^+ \tag{7}$$

$$SO_4^{\bullet-} + OH^- \rightarrow SO_4^{2-} + \bullet OH \tag{8}$$

$$M^{n+} + O_2 \rightarrow M^{(n+1)+} + \bullet O_2^- \tag{9}$$

$$4 \bullet OH \rightarrow {}^1O_2 + 2H_2O \tag{10}$$

$$HSO_5^- \rightarrow SO_3^{\bullet-} + H^+ \tag{11}$$

$$2SO_3^{\bullet-} + H_2O \rightarrow 2HSO_4^- + 1.5^1O_2 \tag{12}$$

3.3.3. DFT calculation for the electronic properties of MnFe₂O₄@HZO

Fukui index and charge distribution of NTMP were calculated using DFT. The Fukui index was used to evaluate the active sites of pollutants. Generally speaking, high f_k^- (electrophilic attack) and f_k° (ROS attack) indicate a high likelihood of electrophilic and ROS attack [54]. N1, P7, P5, H27, H23 and O16 have relatively high f_k° values and are easily attacked by ROS, illustrating that ROS were more inclined to attack C-N

bonds than C-P bonds (Table S7). The highest occupied molecular orbital (HOMO) and lowest unoccupied molecular orbital (LUMO) are the major orbitals involved in the chemical stability of molecule. These orbitals are the basis for characterization of the chemical reactivity and kinetic stability of the molecule [55]. A noteworthy observation is that the HOMO and LUMO orbital energies of NTMP are − 0.1964 and − 0.0287 a.u, respectively (Fig. 6(a-c)). The energy difference between them, termed the energy gap (E_{gap}), is a key indicator for NTMP. Lower E_{gap} values (−0.1677 a.u) mean that NTMP molecule is easier to be stimulated [56]. Notably, $SO_4^{\bullet-}$ (−0.1628 a.u) has a lower LUMO than •OH (−0.15614 a.u), suggesting that $SO_4^{\bullet-}$ had the ability to preferentially accept electrons [55]. The E_{gap} between the LUMO of $SO_4^{\bullet-}$ and the HOMO of NTMP is lower, meaning that electron transfer between $SO_4^{\bullet-}$ and NTMP is more likely to occur, proving that $SO_4^{\bullet-}$ is the dominant ROS.

DFT was used to further verify the active sites of MnFe₂O₄ @HZO for PMS activation (Fig. 6). Fig. S7 displays the stable structures of MnFe₂O₄ and MnFe₂O₄ @HZO, and the relevant HOMO and LUMO models are shown in Fig. 6(d). The HOMO of MnFe₂O₄ is attributable to the electrons on the p orbital of Fe and Mn atoms, while Mn atoms account for the HOMO of MnFe₂O₄ @HZO. MnFe₂O₄ @HZO exhibits a higher HOMO and lower E_{gap} relative to MnFe₂O₄. This shows that it has stronger electron donating ability and easier electron transfer, both attributes imparting higher catalytic performance to the compound [10]. The positive and negative regions of distributions of electrostatic potential (ESP) represent oxidative active site and reductive active site, respectively [57]. Relatively negative potentials are provided around PMS molecule (Fig. 6(e)), while the positive potential is distributed around Fe and Mn atoms in MnFe₂O₄, and the negative charge around the O atom (Fig. 6(f)). Since the electronegativity of Zr atoms differs from that of Fe and Mn atoms, the addition of HZO redistributes the charges in MnFe₂O₄ @HZO. Nonetheless, the positive potential still dwells between the Mn and Fe atoms (Fig. 6(h)). Research shows that the positive charges around Mn atoms are the best attack sites for PMS, meaning that MnFe₂O₄ is the main active center in the MnFe₂O₄ @HZO structure. The potential of Mn atoms is much higher than that of Fe atoms, implying that Mn exchanges charge with PMS more easily. This postulation is supported by the fact that the redox potential of MnOₓ/Mn (II) is higher than that of FeOₓ/Fe(II), evidence of the stronger electron donating ability of MnOₓ.

After PMS is adsorbed on the catalyst, the negative charge mainly appears in the catalyst and the region around PMS molecule (Fig. 6(g, i)). According to Eqs. (S3) and (S4), the adsorption energy (E_{abs1}) of PMS on MnFe₂O₄ is − 1.12 eV, while the E_{abs2} of MnFe₂O₄ @HZO is − 1.86 eV, indicating that chemisorption is the dominant route of adsorption. The higher absolute value of E_{abs} shows higher affinity between PMS and MnFe₂O₄ @HZO, which favors the generation of $SO_4^{\bullet-}$ and $^1O_2$. We also estimated the O-O bond length (l_{O-O}) and O-H bond length (l_{O-H}) before and after PMS adsorption, with the aim of assessing the propensity for O-O bond cleavage and ROS generation [58]. PMS becomes extremely unstable after adsorption on MnFe₂O₄ and MnFe₂O₄ @HZO, while l_{O-O} becomes 3.479 Å and 3.866 Å, respectively. The longer l_{O-O} means that PMS is more likely to generate $SO_4^{\bullet-}$ and •OH after MnFe₂O₄ @HZO adsorption. However, the strong adsorption of H in the O-H bond leads to the cleavage of O-H, which promotes the formation of $SO_5^{\bullet-}$ in the chain reaction, and further generates $^1O_2$ [57]. It is possible that the MnFe₂O₄ @HZO/PMS system accelerates the cleavage of O-O and O-H bonds in PMS, consequently promoting the chain reaction.

3.4. NTMP removal by the MnFe₂O₄@HZO/PMS system under different parameters

3.4.1. Effect of initial pH

NTMP degradation yields a higher quantity of phosphates in the alkaline condition than in the acidic condition (Fig. 7(a)). Phosphates concentration increases first and then decrease at lower pH (<8),
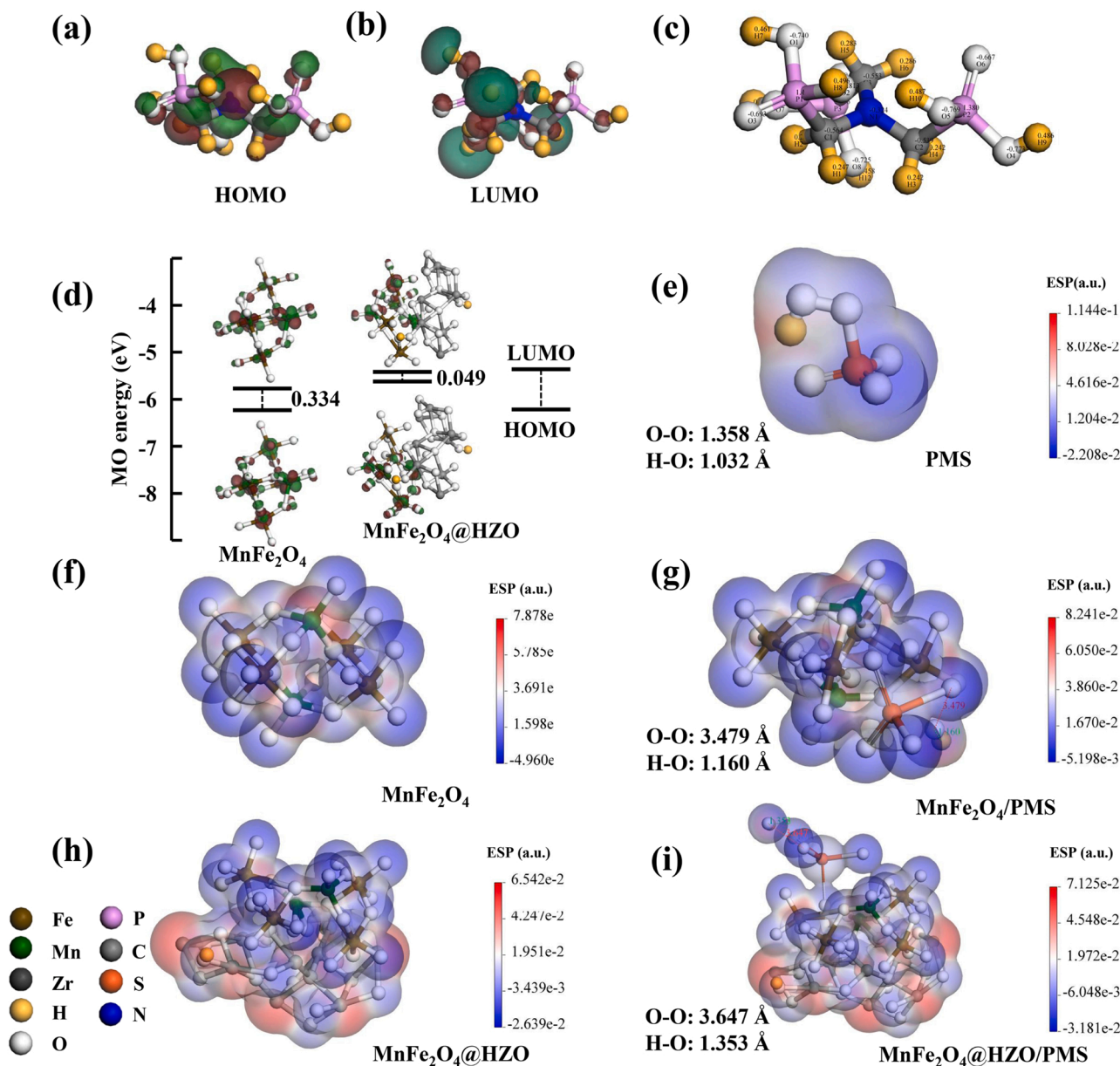
Fig. 6. (a) HOMO, (b) LUMO and (c) the distribution of charges of NTMP. (d) HOMO and LUMO of $MnFe_2O_4$ and $MnFe_2O_4$@HZO. Distributions of electrostatic potential (ESP) for (e) PMS, (f) $MnFe_2O_4$, (g) $MnFe_2O_4$@HZO, (h) $MnFe_2O_4$/PMS and (i) $MnFe_2O_4$@HZO/PMS models.

showing alkaline environment is not available for phosphates adsorption by $MnFe_2O_4$ @HZO. Higher TP removal efficiency can thus be achieved (94.5%−91.7%) at pH_0 3–7 (Fig. 7(b)). When pH_0 continues to rise, TP removal efficiency declines significantly, reaching a meager 20.86% at pH_0 11. The relevant k_{obs} also declines from 0.122 to 0.016 min^{-1}, demonstrating that the system has better NTMP removal efficiency under acidic and neutral conditions. The leaching concentration of Fe, Mn and Zr ions remain < 0.6 mg/L at $pH_0 \geq 6$ after reaction (Fig. S8), further strengthening the stability of $MnFe_2O_4$ @HZO.

At lower pH, NTMP degradation rate at the initial stage of reaction was faster, while the adsorption rate of HZO on phosphates was relatively slow, which led to an upward trend of phosphates concentration. Subsequently, as the reaction proceeded, the amount of released phosphates became less and the concentration of accumulated phosphates in the system dropped based on the slow adsorption of HZO shell. According to the results of zeta potential analysis, pH_{PZC} value of $MnFe_2O_4$ @HZO is 5.52 (Fig. S9). The hydroxyl groups on the surface of $MnFe_2O_4$ @HZO were protonated and positively charged, which was favorable for

the adsorption of negatively charged phosphates at lower pH [20]. Deprotonation of surface hydroxyl groups imparted a negative charge on $MnFe_2O_4$ @HZO at pH values greater than 5.52. Owing to the effect of Donnan co-ion repulsion or electrostatic repulsion, phosphates were not easily adsorbed by catalyst [59]. Therefore, in the early stage of reaction, the phosphates produced by NTMP decomposition rapidly accumulated and were simultaneously adsorbed. $MnFe_2O_4$ @HZO could effectively capture phosphates at lower pH environment within short periods. NTMP has six pK_a values, which are 0.3, 1.5, 4.6, 5.9, 7.3 and 12.1, while the pK_{a2} of PMS is 9.4 [36]. This indicates that $MnFe_2O_4$ @HZO with more positive charges would have stronger affinity for PMS under acidic conditions. In contrast, negatively charged catalyst was unfavorable for the adsorption of HSO_5^-, SO_5^{2-} and NTMP under basic conditions. Of note, the dominant species of PMS at pH< 9.4 was HSO_5^-, which accelerated $^1O_2$ production and consequently the catalytic rate [60]. However, the dominant species of PMS was SO_5^{2-} with weak oxidizing ability. This is the reason why NTMP removal efficiency would be lower under strongly basic condition.
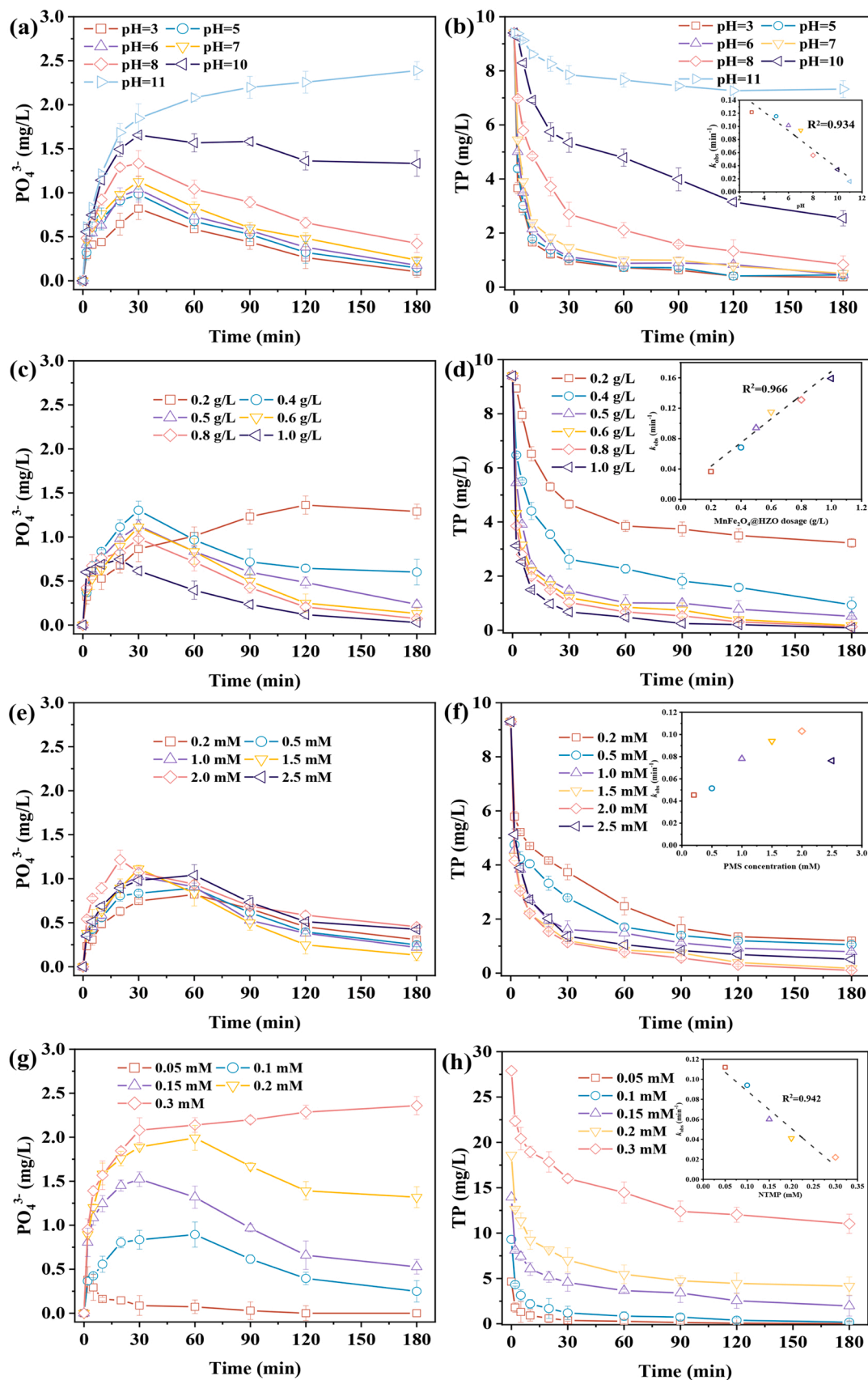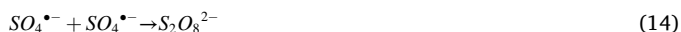
Fig. 7. NTMP removal in different conditions: (a, b) pH$_0$ (35 °C, [NTMP]$_0$ = 0.1 mM (9.3 mg TP/L), [PMS]$_0$ = 1.5 mM, MnFe$_2$O$_4$@HZO dose= 0.5 g/L), (c, d) MnFe$_2$O$_4$@HZO dose (35 °C, pH$_0$ 7, [NTMP]$_0$ = 0.1 mM (9.3 mg TP/L), [PMS]$_0$ = 1.5 mM), (e, f) PMS concentration (35 °C, pH$_0$ 7, [NTMP]$_0$ = 0.1 mM (9.3 mg TP/L), MnFe$_2$O$_4$ @HZO dose= 0.6 g/L), and (g, h) NTMP concentration (35 °C, pH$_0$ 7, [PMS]$_0$ = 1.5 mM, MnFe$_2$O$_4$@HZO dose= 0.6 g/L).

3.4.2. Effects of MnFe₂O₄@HZO dose and PMS concentration

Phosphates continue to accumulate in the process, when MnFe₂O₄@HZO dose is 0.2 g/L (Fig. 7(c)). However, the amount of phosphates increases first and then declines slowly. As MnFe₂O₄@HZO dose increases from 0.4 g/L to 1.0 g/L, the relevant TP removal efficiency improves from 65.9% (0.037 min⁻¹) to 99.1% (0.159 min⁻¹) (Fig. 7(d)). TP removal efficiency can reach 96.5%, leaving a TP concentration of only 0.18 mg/L in solution, when MnFe₂O₄@HZO dose is 0.6 g/L. The addition of catalyst can activate PMS, degrading NTMP to generate large amounts of phosphates within a short time. Notably, the adsorption rate for phosphates was much lower than that for NTMP. 0.2 g/L of MnFe₂O₄@HZO was insufficient to adsorb the large amount of phosphates produced, indicating the need for a higher dose to achieve the desired catalysis and adsorption. On one hand, it could activate PMS to generate more ROS to accelerate NTMP degradation [19]. On the other hand, it was able to promote the adsorption effect of phosphates and prevent diffusion into the solution [61].

Adsorption experiments were carried out to evaluate the adsorption effect of MnFe₂O₄@HZO, MnFe₂O₄ core and HZO shell on the system (Fig. S10(a-c)). Although MnFe₂O₄ and HZO individually have lower adsorption efficiencies for NTMP than MnFe₂O₄@HZO, the adsorption efficiency of MnFe₂O₄ is better than that of HZO. In addition, we controlled the pH of solution after reaction to 11, and kept stirring for 3 h to achieve phosphorus desorption. It was observed that phosphate concentration rose to 6.73 mg/L, but the TP concentration remained a meager 7.81 mg/L. This can be attributed to incomplete desorption of phosphates or phosphorus-containing byproducts. It can thus be safely stated that MnFe₂O₄@HZO has preferential adsorption capacity for phosphates.

As shown in Fig. 7(e), phosphates generation shows a trend of increasing first and then decreasing under different PMS concentrations. TP removal efficiency improves from 85% (0.045 min⁻¹) to 97.8% (0.103 min⁻¹) when PMS concentration grows from 0.2 to 2 mM (Fig. 7(f)). 96.5% of TP removal efficiency can be achieved with the addition of 1.5 mM PMS, although further increases in PMS concentration do not improve the TP removal efficiency and k_{obs}. However, the decomposition rate of NTMP to phosphates is slow in the range of 0.2–0.5 mM PMS, which retards NTMP degradation. The catalytic active sites on the surface of MnFe₂O₄@HZO tend to be saturated, which makes the accumulation rate of phosphates faster than that of PMS, resulting in an earlier inflection point [36]. However, excess PMS could not be fully activated owing to the limited number of active sites on the catalyst surface. Instead, HSO_5^- had a scavenging effect on $SO_4^{\bullet-}$ [62] (Eq. (13)). Excess $SO_4^{\bullet-}$ also consumed •OH and $SO_4^{\bullet-}$ through self-quenching, generating the less active HSO_5^- and $S_2O_8^{2-}$ (Eqs. (14) and (15)) [63]. In a nutshell, the negative effects of excess PMS dose should be considered in the actual ICCW treatment process.

$$SO_4^{\bullet-} + HSO_5^- \rightarrow SO_5^{\bullet-} + SO_4^{2-} + H^+ \tag{13}$$

$$SO_4^{\bullet-} + SO_4^{\bullet-} \rightarrow S_2O_8^{2-} \tag{14}$$

$$HO^{\bullet} + SO_4^{\bullet-} \rightarrow HSO_5^- \tag{15}$$
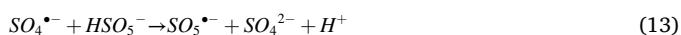
3.4.3. Effects of NTMP concentration and temperature

The amount of phosphates generated during the reaction increases considerably with rising NTMP concentrations (Fig. 7(g)). The generation of phosphates still shows a trend of rapid increase firstly and then slow decrease, particularly when initial NTMP concentration is low (0.05–0.2 mM). Consequently, increase of NTMP concentration from 0.05 to 0.3 mM causes TP removal efficiency to decrease from 99.9% (0.112 min⁻¹) to 58.1% (0.022 min⁻¹) (Fig. 7(h)). On one hand, $SO_4^{\bullet-}$ would be consumed by the accumulated phosphates, thereby reducing NTMP degradation rate [64]. On the other hand, the competitive adsorption between phosphates and NTMP impedes the adsorptive capability of MnFe₂O₄@HZO for the released phosphates, specifically at elevated NTMP levels. Therefore, high-concentrations of NTMP at the beginning of the reaction resulted in higher concentrations of phosphates released into solution.

TP removal efficiencies of different temperatures were investigated to evaluate the effects of temperature on the NTMP degradation. As the reaction temperature increases, the degradation rate of NTMP improves from 0.031 min⁻¹ (25 °C) to 0.11 min⁻¹ (45 °C) (Fig. S11). The endothermic nature of the reaction involving ROS could account for this observation. Besides, temperature rises in the reaction system can noticeably accelerate the thermal motion between molecules and raise the likelihood of intermolecular collision. The activation energy (E_a) of the system was determined to be 23.3 kJ/mol (according to Arrhenius equation) [65]. The lower E_a value means that MnFe₂O₄@HZO exhibits excellent catalytic performance. It is worth noting that the calculated E_a value is much higher than the diffusion-controlled reaction (10–13 kJ/mol), and the apparent reaction rate of this system is mainly controlled by chemical reaction rate on the surface of MnFe₂O₄@HZO, rather than mass transfer rate.

### 3.5. Applicability of the MnFe₂O₄@HZO/PMS system

3.5.1. Effects of coexisting substances and simulated water matrix

Coexisting substances in industrial wastewater not only consume ROS, but may also compete with the generated $H_2PO_4^-/HPO_4^{2-}$ for adsorption on the surface of MnFe₂O₄/HZO [61]. The order of inhibition intensity for TP removal by these matrices was as follows: HCO_3^- (0.025 min⁻¹)>SO_4^{2-} (0.064 min⁻¹)>HA (0.064min⁻¹)>Cl^- (0.065 min⁻¹)>NO_3^- (0.103 min⁻¹) (Fig. 8(a)). NO_3^-, Cl^- and SO_4^{2-} do not inhibit TP removal in the concentration range of 0.1–20 mM, while TP removal efficiencies remain above 85%. At a low-concentration, HCO_3^- (0.1–1 mM) also have minimal inhibitory effect. However, the rising concentrations of HCO_3^- (5–20 mM) may exacerbate the inhibitory effect. Notably, TP removal efficiency decreases from initial 96.5–39.0% with 20 mM HCO_3^-. Inhibition of phosphates removal by SO_4^{2-} and HCO_3^- (>5 mM) is negligible and only occurs at high concentrations of the species. Although different concentrations of HA have no impact on TP removal, phosphates adsorption dropped markedly with increasing HA concentration.

Anions in the aqueous solution will react with ROS in the oxidation reaction, hampering the activation efficiency of the catalyst for PMS [66]. PMS activation by Cl^- and NO_3^- inhibition was mainly because they reacted with $SO_4^{\bullet-}$ or •OH to generate less active species $NO_3^{\bullet}$ ($E_{(NO3\bullet/NO3-)}= 2$–2.2 V), $Cl^{\bullet}$, $Cl_2^{\bullet-}$ and $HOCl^{\bullet-}$ ($E_{(Cl\bullet/Cl-)}= 2.4$ V, $E_{(Cl2\bullet/Cl-)}= 2.0$ V, $E_{(HOCl\bullet-/Cl-)}= 1.48$ V) [67]. Interestingly, the redox potential of these radicals was lower than that of $SO_4^{\bullet-}$ and •OH, indicating that the presence of NO_3^- and Cl^- had a certain inhibitory effect on the oxidation system [66]. High-concentration SO_4^{2-} reduced the redox potential of $SO_4^{\bullet-}/SO_4^{2-}$, resulting in a decrease in the activation efficiency of PMS [68]. HCO_3^- also retarded PMS activation, possibly reacting with $SO_4^{\bullet-}$ or •OH to form $CO_3^{\bullet-}$ [69]. On the other hand, HCO_3^- with strong buffering capacity could inhibit and reduce the oxidation potential of ROS by increasing the solution pH [70]. Furthermore, HA might compete with NTMP for ROS, decreasing the TP removal efficiency as a result.

During the adsorption reaction, anions competed with $H_2PO_4^-/HPO_4^{2-}$ for adsorption on the surface of MnFe₂O₄@HZO, consequently lowering the adsorption efficiency of phosphates. It is likely that SO_4^{2-} formed an inner-sphere complex on the surface of MnFe₂O₄@HZO, while Cl^- and NO_3^- formed a less competitive outer-sphere complex [61]. Anions with larger charge were more competitive with phosphates during adsorption process, in the following order of inhibition effect: SO_4^{2-}>Cl^->NO_3^- (Fig. S12). HCO_3^- with stronger buffering capacity may have increased solution pH, deprotonating and conferring a negative charge on the MnFe₂O₄@HZO surface. Phosphates with negative charge were thus less adsorbed. Although only a limited quantity of Zr-HA was formed, the high HA concentration had no obvious effect on phosphates
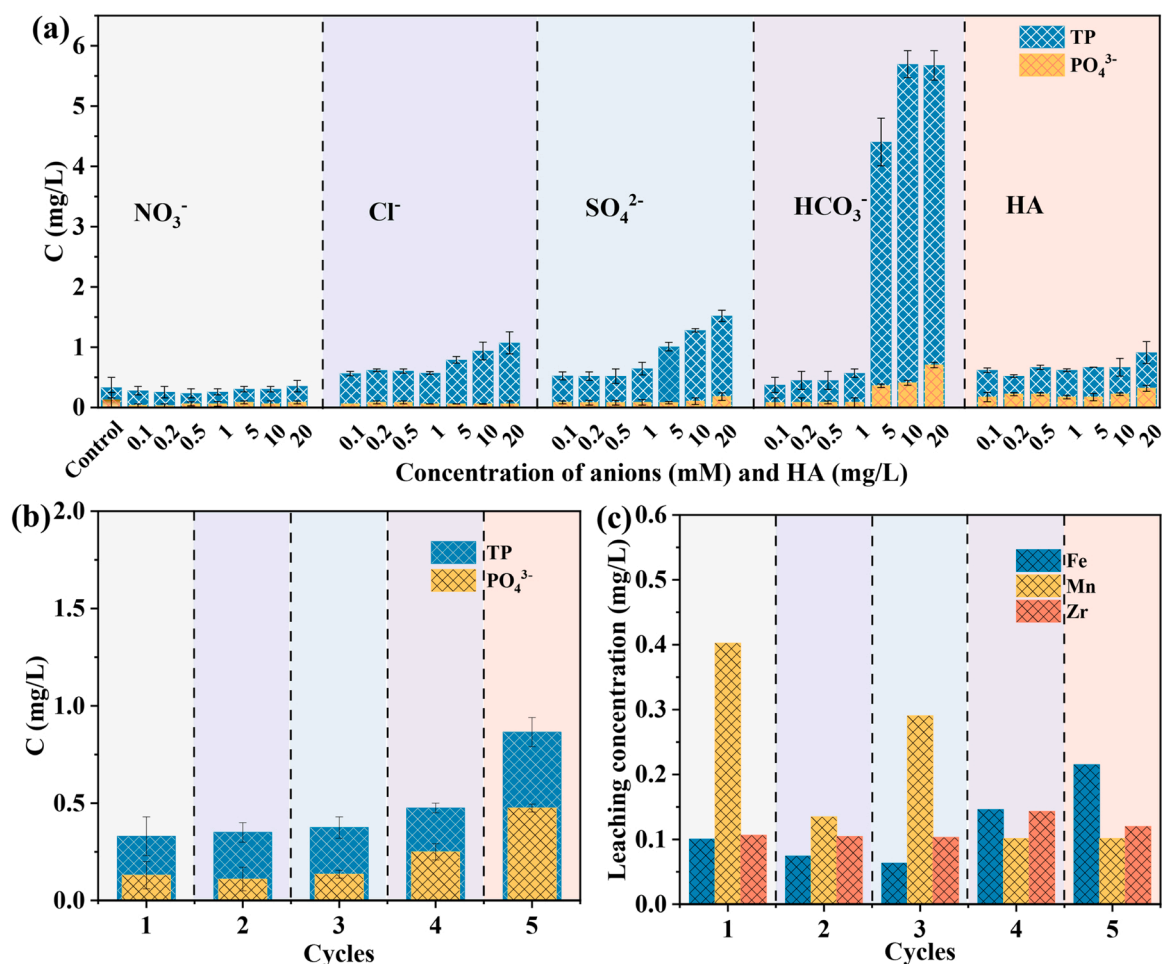
Fig. 8. (a) Effect of the coexisting substances on NTMP removal. (b, c) Five cycles of $MnFe_2O_4$@HZO for NTMP removal and leaching of ions. (35 °C, pH_0 7, $[NTMP]_0$ = 0.1 mM (9.3 mg TP/L), $[PMS]_0$ = 1.5 mM, $MnFe_2O_4$ @HZO dose = 0.6 g/L).

adsorption, because HA molecules with larger molecular weight were unable to enter the internal pores of $MnFe_2O_4$ @HZO [1].

Three typical phosphonates (PBTC, HEDP and EDTMP) were selected to assess the effectiveness of system. Detailed molecular structures are provided in Table S8. TP concentrations of all contaminants fell below 1.8 mg/L within 180 min (Fig. S13(a)), while the quantity of generated phosphates after degradation did not exceed 0.3 mg/L (Fig. S13(b)). It can be seen that this system also has great decontamination performance for other phosphonates. We also verified the feasibility of system for NTMP removal in practical application. TP removal efficiency still reaches 82.8% in the simulated ICCW and has a higher k_{obs}. The remaining TP concentration is a measly 1.6 mg/L (Fig. S14). In conclusion, it is clear that high-concentrations of HCO_3^-, alongside anions and HA, have an inhibitory effect on oxidation and adsorptive properties of the system. The $MnFe_2O_4$ @HZO/PMS system has a better ability to resist the interference of water matrix, and possesses a huge application prospect in the actual treatment of ICCW.

3.5.2. Reusability and stability of $MnFe_2O_4$@HZO

Reusability and stability have important implications for practical application of catalysts in wastewater treatment. NTMP (TP and phosphates) removal efficiency remains above 90% after five cycles (Fig. 8 (b)), demonstrating the reusability of system. During each magnetic recovery process, reaction system maintains higher catalyst recovery (>92%) (Fig. S15). Metal leaching concentrations are detected in each cycle, the highest leaching concentrations of Fe, Mn and Zr ions reaching 0.22, 0.4 and 0.14 mg/L in the five cycles at pH_0 7, respectively (Fig. 8

(c)). Though Mn leaching concentration can be relatively high, it still falls below the Level I threshold (2.0 mg/L) of comprehensive emissions for sewage (GB 8978–1996) (China) [71]. Since Fe and Zr are non-toxic metals, the negligible amounts of these elements that leach pose no danger to the environment.

XRD diffraction peak intensities of both fresh and exhausted $MnFe_2O_4$ @HZO gradually decline after one cycle and five cycles, likely due to the persistent passivation of the catalyst surface during degradation process (Fig. S16). The relevant variation of saturation magnetization from initial 49.7–50.2 emu/g after one cycle, revealed that the magnetic intensity of the catalyst was unaffected during NTMP degradation (Fig. S17). Excitingly, exhausted $MnFe_2O_4$/HZO still maintains the intact spherical structure, as the catalysis and adsorption processes do not affect the morphology of the catalyst (Fig. S18(a-b)). In conclusion, $MnFe_2O_4$/HZO exhibits great regeneration and reuse performance.

3.6. Removal pathways of NTMP and toxicity analysis

The intermediates of the degradation process were detected and analysed to elucidate the pathways of NTMP degradation. IDMP and AMPA were detected through the pre-column FMOC-Cl derivatization (Fig. S19). LC-MS also confirmed the presence of dominating hydroxymethylphosphonic acid (HMP), as shown in Fig. S20 and Table S9. Inorganic anions, e.g., NH_3-N and NO_3^--N, were detected in the final degradation (Fig. S21). Interestingly, NH_3-N and NO_3^--N concentrations begin to increase rapidly at 20 min, and both reach their highest at 0.94 and 0.51 mg/L at 60 min, respectively. A lag period exists in the

production of NH_3-N and NO_3^--N, reflecting that C-N cleavage in NTMP was preferred to C-P bonding. More importantly, there is a longer lag period in the generation of HCOOH, as its molecular signal increases rapidly from 0.011 μS•min at 60 min to 0.15 μS•min at 100 min (Fig. S22). This result implied that the intermediate was further converted to HCOOH after C-P bond cleavage [37]. Finally, TOC concentration was reduced from 3.65 mg/L to 2.12 mg/L within 180 min in the system, while mineralization efficiency of NTMP reached 41.9% (Fig. S23).

Based on these results, we proposed the degradation pathways of NTMP (Fig. 9(a)). ROS were crucial to NTMP degradation in the system. Firstly, a C-N bond in the NTMP molecule was cleaved to form IDMP and HMP, and a C-N bond in IDMP cleaved again to form AMPA and HMP [1]. Then, the last C-N bond in AMPA molecule was broken to generate NH_3-N, NO_3^--N and HMP [37]. Three HMP molecules were generated in

the process of C-N bond cleavage. Owing to variation of the HCOOH molecular signal, it has been postulated that HMP was converted into CH_3OH, CH_2O and HCOOH successively, the C-P bond was cleaved to release H_3PO_4, and the HMP molecule was converted into CH_3OH [1]. Ultimately, the HCOOH molecule was further mineralized into CO_2 and H_2O. For the $MnFe_2O_4$ @HZO/PMS system, $MnFe_2O_4$ core acted as the catalytic medium to activate PMS to generate ROS, where Mn and Fe species served as active centers to provide electrons to PMS, and ROS dominated by $SO_4^{\bullet-}$ (radical degradation) and $^1O_2$ (non-radical degradation) accelerated the degradation of NTMP (Fig. 9(b)). The phosphates products generated during the degradation process were simultaneously adsorbed by the inner-sphere complexation of HZO shell. Finally, the reaction system achieved integral removal of NTMP.

Acute toxicity of *Tetrahymena (T). pyriformis* (50% inhibition growth concentration (IGC50) in 48 h), developmental toxicity and
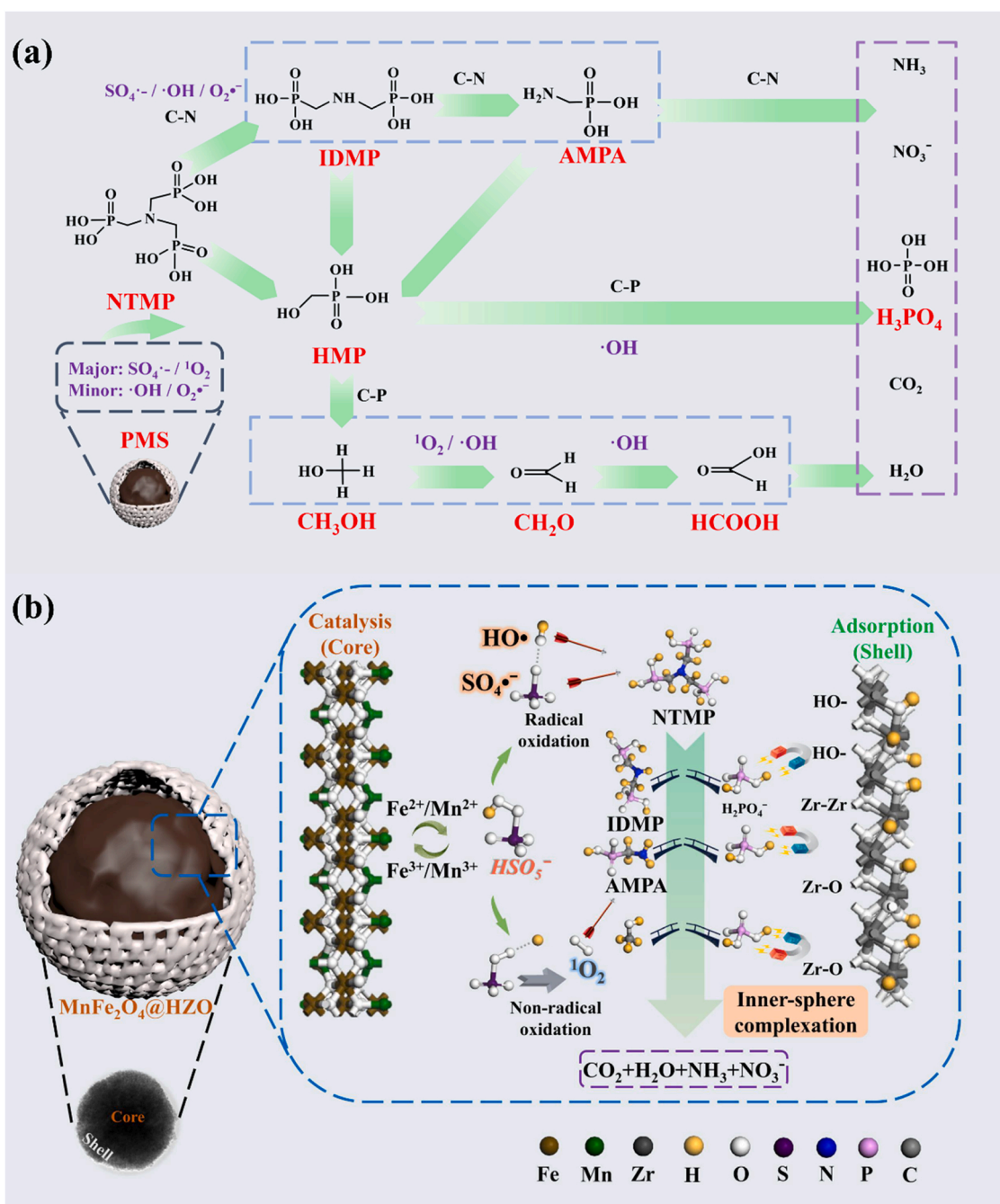

Fig. 9. (a) Degradation pathways and (b) integral removal process of NTMP by $MnFe_2O_4$@HZO/PMS system.

mutagenicity of NTMP intermediates were evaluated using toxicity assessment software (T.E.S.T.) to understand the relevant environmental impact [72]. Fig. S24 shows the ecotoxicity results of these intermediates and NTMP. The median lethal dose (LD$_{50}$) of NTMP for a rat is 4830.8 mg/kg, which is much higher than all intermediates (Fig. S24 (a)). IGC50 results revealed significant increases in the toxicities of CH$_2$ and IDMP, but negligible toxicity of the other intermediates. This indicated that NTMP degradation can effectively control the acute toxicity (Fig. S24(b)). More importantly, comparison of the bioconcentration factors of intermediates with NTMP showed that concentrations of the intermediates consistently fell, except for the bioconcentration factors of CH$_3$OH and CH$_2$O (Fig. S24(c)). Similar to acute toxicity, NTMP of mutagenicity positive was converted to negative intermediates during the reaction (Fig. S24(d)). Therefore, although some intermediates retained their growth inhibitory effects, they greatly alleviated environmental hazards.

4. Conclusions

In this study, core-shell MnFe$_2$O$_4$ @HZO was prepared using a sol-gel method, which HZO particles were uniformly coated on the surface of MnFe$_2$O$_4$ spheres through an electrostatic force. The MnFe$_2$O$_4$ @HZO/ PMS system was created via "adsorption-catalysis-adsorption", the redox electron transfer between Fe(II)/Fe(III) and Mn(II)/Mn(III) played an important role in PMS activation. A stable internal coordination complex can be obtained with H$_2$PO$_4^-$/HPO$_4^{2-}$ mainly via -Zr-OH bonds. Quenching experiment and EPR analysis indicated the contributions of ROS followed the order: SO$_4^{\bullet-}$>^{1}O$_2$ > •OH>O$_2^{\bullet-}$. DFT calculation further confirmed that the MnFe$_2$O$_4$ @HZO/PMS system can accelerate the cleavage of O-O and O-H bonds in PMS, and thus promote the chain reaction. Furthermore, the oxidation of system for NTMP is largely impeded by high-concentrations of HCO$_3^-$. In simulated ICCW, TP removal efficiency still reached 82.8%, demonstrating that catalysis was potent enough and facilitated the success of the reaction.

CRediT authorship contribution statement

Shunlong Pan: Visualization, Investigation. **Xinrui Guo**: Visualization, Investigation. **Xing Lu**: Visualization, Investigation. **Rong Li**: Visualization, Investigation. **Hao Hu**: Conceptualization, Methodology, Software, Data curation, Writing – original draft, Supervision, Validation, Writing – review & editing. **Xi Nie**: Conceptualization, Methodology, Software, Data curation, Writing – original draft, Writing – review & editing. **Biming Liu**: Conceptualization, Methodology, Software. **Rong Chen**: Conceptualization, Methodology, Supervision, Software, Validation. **Mingxin Zhu**: Methodology, Software. **Shengqiang Hei**: Software, Data curation. **Xianzheng Zhu**: Data curation, Writing – original draft, Supervision. **Shuo Zhang**: Supervision, Validation, Writing – review & editing. **Hua Zhou**: Conceptualization, Methodology, Software.

Declaration of Competing Interest

The authors declare that they have no known competing financial interests or personal relationships that could have appeared to influence the work reported in this paper.

Data availability

The data that has been used is confidential.

References

[1] S. Sun, S. Wang, Y. Ye, B. Pan, Highly efficient removal of phosphonates from water by a combined Fe(III)/UV/co-precipitation process, Water Res. 153 (2019) 21–28.
[2] E. Rott, H. Steinmetz, J.W. Metzger, Organophosphonates: a review on environmental relevance, biodegradability and removal in wastewater treatment plants, Sci. Total Environ. 615 (2018) 1176–1191.
[3] X. Zhang, J. Li, W.-Y. Fan, G.-P. Sheng, Photomineralization of effluent organic phosphorus to orthophosphate under simulated light illumination, Environ. Sci. Technol. 53 (2019) 4997–5004.
[4] E. Rott, M. Nouri, C. Meyer, R. Minke, M. Schneider, K. Mandel, A. Drenkova-Tuhtan, Removal of phosphonates from synthetic and industrial wastewater with reusable magnetic adsorbent particles, Water Res. 145 (2018) 608–617.
[5] X. Liu, F. Huang, Y. Yu, P. Zhao, Y. Zhou, Y. He, Y. Xu, Y. Zhang, Ofloxacin degradation over Cu–Ce tyre carbon catalysts by the microwave assisted persulfate process, Appl. Catal. B Environ. 253 (2019) 149–159.
[6] P. Hu, M. Long, Cobalt-catalyzed sulfate radical-based advanced oxidation: a review on heterogeneous catalysts and applications, Appl. Catal. B Environ. 181 (2016) 103–117.
[7] S. Xiao, M. Cheng, H. Zhong, Z. Liu, Y. Liu, X. Yang, Q. Liang, Iron-mediated activation of persulfate and peroxymonosulfate in both homogeneous and heterogeneous ways: a review, Chem. Eng. J. 384 (2020), 123265.
[8] J. Rodríguez-Chueca, S. Guerra-Rodríguez, J.M. Raez, M.-J. López-Muñoz, E. Rodríguez, Assessment of different iron species as activators of S2O82- and HSO5- for inactivation of wild bacteria strains, Appl. Catal. B Environ. 248 (2019) 54–61.
[9] L. Chen, X. Zuo, S. Yang, T. Cai, D. Ding, Rational design and synthesis of hollow Co3O4@Fe2O3 core-shell nanostructure for the catalytic degradation of norfloxacin by coupling with peroxymonosulfate, Chem. Eng. J. 359 (2019) 373–384.
[10] J. Liu, Q. Chen, Y. Yang, H. Wei, M. Laipan, R. Zhu, H. He, M.F. Hochella, Coupled redox cycling of Fe and Mn in the environment: the complex interplay of solution species with Fe- and Mn-(oxyhydr)oxide crystallization and transformation, Earth-Sci. Rev. 232 (2022), 104105.
[11] G.-X. Huang, C.-Y. Wang, C.-W. Yang, P.-C. Guo, H.-Q. Yu, Degradation of bisphenol A by peroxymonosulfate catalytically activated with Mn1.8Fe1.2O4 nanospheres: synergism between Mn and Fe, Environ. Sci. Technol. 51 (2017) 12611–12618.
[12] H. Qin, Y. Yang, W. Shi, Y. She, Heterogeneous Fenton degradation of ofloxacin catalyzed by magnetic nanostructured MnFe2O4 with different morphologies, Environ. Sci. Pollut. Res. 28 (2021) 26558–26570.
[13] X. Zhang, B. Xu, S. Wang, X. Li, C. Wang, B. Liu, F. Han, Y. Xu, P. Yu, Y. Sun, Tetracycline degradation by peroxymonosulfate activated with CoNx active sites: performance and activation mechanism, Chem. Eng. J. 431 (2022) 133477.
[14] J. Lin, Y. Zhan, H. Wang, M. Chu, C. Wang, Y. He, X. Wang, Effect of calcium ion on phosphate adsorption onto hydrous zirconium oxide, Chem. Eng. J. 309 (2017) 118–129.
[15] L. Fang, B. Wu, I.M.C. Lo, Fabrication of silica-free superparamagnetic ZrO2@ Fe3O4 with enhanced phosphate recovery from sewage: Performance and adsorption mechanism, Chem. Eng. J. 319 (2017) 258–267.
[16] S. Shan, H. Tang, Y. Zhao, W. Wang, F. Cui, Highly porous zirconium-crosslinked graphene oxide/alginate aerogel beads for enhanced phosphate removal, Chem. Eng. J. 359 (2019) 779–789.
[17] M. Zhang, C. Wang, C. Liu, R. Luo, J. Li, X. Sun, J. Shen, W. Han, L. Wang, Metal–organic framework derived Co3O4/C@SiO2 yolk–shell nanoreactors with enhanced catalytic performance, J. Mater. Chem. A 6 (2018) 11226–11235.
[18] S. Xing, D. Zhao, W. Yang, Z. Ma, Y. Wu, Y. Gao, W. Chen, J. Han, Fabrication of magnetic core–shell nanocomposites with superior performance for water treatment, J. Mater. Chem. A 1 (2013) 1694–1700.
[19] S. Zhang, H. Gao, X. Xu, R. Cao, H. Yang, X. Xu, J. Li, MOF-derived CoN/N-C@SiO2 yolk-shell nanoreactor with dual active sites for highly efficient catalytic advanced oxidation processes, Chem. Eng. J. 381 (2020) 122670.
[20] A. Sarkar, S.K. Biswas, P. Pramanik, Design of a new nanostructure comprising mesoporous ZrO2 shell and magnetite core (Fe3O4@mZrO2) and study of its phosphate ion separation efficiency, J. Mater. Chem. 20 (2010) 4417–4424.
[21] T. Zeng, X. Zhang, S. Wang, H. Niu, Y. Cai, Spatial confinement of a Co3O4 catalyst in hollow metal–organic frameworks as a nanoreactor for improved degradation of organic pollutants, Environ. Sci. Technol. 49 (2015) 2350–2357.
[22] Y. Zhang, F. Gao, B. Wanjala, Z. Li, G. Cernigliaro, Z. Gu, High efficiency reductive degradation of a wide range of azo dyes by SiO2-Co core-shell nanoparticles, Appl. Catal. B Environ. 199 (2016) 504–513.
[23] Y. Yao, Y. Cai, F. Lu, F. Wei, X. Wang, S. Wang, Magnetic recoverable MnFe2O4 and MnFe2O4-graphene hybrid as heterogeneous catalysts of peroxymonosulfate activation for efficient degradation of aqueous organic pollutants, J. Hazard. Mater. 270 (2014) 61–70.

[24] Z. Liu, Z. Gao, Q. Wu, Activation of persulfate by magnetic zirconium-doped manganese ferrite for efficient degradation of tetracycline, Chem. Eng. J. 423 (2021), 130283.

[25] M. Hájek, J. Kocík, K. Frolich, A. Vávra, Mg-Fe mixed oxides and their rehydrated mixed oxides as catalysts for transesterification, J. Clean. Prod. 161 (2017) 1423–1431.

[26] Q. Tang, L. Jiang, J. Liu, S. Wang, G. Sun, Effect of surface manganese valence of manganese oxides on the activity of the oxygen reduction reaction in alkaline media, ACS Catal. 4 (2014) 457–463.

[27] D. Wilson, M.A. Langell, XPS analysis of oleylamine/oleic acid capped Fe3O4 nanoparticles as a function of temperature, Appl. Surf. Sci. 303 (2014) 6–13.

[28] M. Mallet, K. Barthélémy, C. Ruby, A. Renard, S. Naille, Investigation of phosphate adsorption onto ferrihydrite by X-ray photoelectron spectroscopy, J. Colloid Interface Sci. 407 (2013) 95–101.

[29] J. Luo, X. Luo, J. Crittenden, J. Qu, Y. Bai, Y. Peng, J. Li, Removal of antimonite (Sb (III)) and antimonate (Sb(V)) from aqueous solution using carbon nanofibers that are decorated with zirconium oxide (ZrO2), Environ. Sci. Technol. 49 (2015) 11115–11124.

[30] J. Deng, S. Feng, X. Ma, C. Tan, H. Wang, S. Zhou, T. Zhang, J. Li, Heterogeneous degradation of Orange II with peroxymonosulfate activated by ordered mesoporous MnFe2O4, Sep. Purif. Technol. 167 (2016) 181–189.

[31] Y. Chen, Z. Zeng, Y. Li, Y. Liu, Y. Chen, Y. Wu, J. Zhang, H. Li, R. Xu, S. Wang, Z. Peng, Glucose enhanced the oxidation performance of iron-manganese binary oxides: structure and mechanism of removing tetracycline, J. Colloid Interface Sci. 573 (2020) 287–298.

[32] R.M. Freire, T.S. Ribeiro, I.F. Vasconcelos, J.C. Denardin, E.B. Barros, G. Mele, L. Carbone, S.E. Mazzetto, P.B.A. Fechine, MZnFe2O4 (M = Ni, Mn) cubic superparamagnetic nanoparticles obtained by hydrothermal synthesis, J. Nanopart. Res. 15 (2013) 1616.

[33] A. Sivakumar, S. Sahaya Jude Dhas, P. Sivaprakash, A.I. Almansour, R. Suresh Kumar, N. Arumugam, K. Perumal, S. Arumugam, S.A. Martin Britto Dhas, Raman spectroscopic and electrochemical measurements of dynamic shocked MnFe2O4 nano-crystalline materials, J. Inorg. Organomet. Polym. Mater. 32 (2022) 344–352.

[34] P.R. Martin, D. Buchner, M.A. Jochmann, M. Elsner, S.B. Haderlein, Two pathways compete in the Mn(II)-catalyzed oxidation of aminotrismethylene phosphonate (ATMP), Environ. Sci. Technol. 56 (2022) 4091–4100.

[35] J. Hai, L. Liu, W. Tan, R. Hao, G. Qiu, Catalytic oxidation and adsorption of Cr(III) on iron-manganese nodules under oxic conditions, J. Hazard. Mater. 390 (2020), 122166.

[36] W. Zheng, Y. Sun, Y. Gu, Assembly of UiO-66 onto Co-doped Fe3O4 nanoparticles to activate peroxymonosulfate for efficient degradation of fenitrothion and simultaneous in-situ adsorption of released phosphate, J. Hazard. Mater. 436 (2022), 129058.

[37] Z. Wang, G. Chen, S. Patton, C. Ren, J. Liu, H. Liu, Degradation of nitrilotris-methylenephosphonic acid (NTMP) antiscalant via persulfate photolysis: implications on desalination concentrate treatment, Water Res. 159 (2019) 30–37.

[38] J. Zhu, S. Wang, H. Li, J. Qian, L. Lv, B. Pan, Degradation of phosphonates in Co (II)/peroxymonosulfate process: performance and mechanism, Water Res. 202 (2021), 117397.

[39] X. Zhang, Y. Wang, M. Feng, G.-E. Yuan, Comparison of electrocoagulation and chemical coagulation in removal of phosphonate chelators from water, Water Sci. Technol. 85 (2022) 2015–2026.

[40] L. Yu, G. Zhang, C. Liu, H. Lan, H. Liu, J. Qu, Interface stabilization of undercoordinated iron centers on manganese oxides for nature-inspired peroxide activation, ACS Catal. 8 (2018) 1090–1096.

[41] H. Fu, S. Ma, P. Zhao, S. Xu, S. Zhan, Activation of peroxymonosulfate by graphitized hierarchical porous biochar and MnFe2O4 magnetic nanoarchitecture for organic pollutants degradation: structure dependence and mechanism, Chem. Eng. J. 360 (2019) 157–170.

[42] Z. Wang, X. Xu, X. Liang, C. Lei, Y. Cui, W. Wu, Y. Yang, Z. Zhang, Z. Lei, Construction of heterostructured MIL-125/Ag/g-C3N4 nanocomposite as an efficient bifunctional visible light photocatalyst for the organic oxidation and reduction reactions, Appl. Catal. B Environ. 205 (2017) 42–54.

[43] X. Li, R. Lv, W. Zhang, M. Li, J. Lu, Y. Ren, Y. Yin, J. Liu, Amorphous zirconium oxide activates peroxymonosulfate for selective degradation of organic compounds: Performance, mechanisms and structure-activity relationship, Water Res. 228 (2023), 119363.

[44] J. Li, L. Yang, B. Lai, C. Liu, Y. He, G. Yao, N. Li, Recent progress on heterogeneous Fe-based materials induced persulfate activation for organics removal, Chem. Eng. J. 414 (2021), 128674.

[45] W.-D. Oh, Z. Dong, T.-T. Lim, Generation of sulfate radical through heterogeneous catalysis for organic contaminants removal: current development, challenges and prospects, Appl. Catal. B Environ. 194 (2016) 169–201.

[46] Q. Zhang, J. Teng, G. Zou, Q. Peng, Q. Du, T. Jiao, J. Xiang, Efficient phosphate sequestration for water purification by unique sandwich-like MXene/magnetic iron oxide nanocomposites, Nanoscale 8 (2016) 7085–7093.

[47] H. Qiu, C. Liang, X. Zhang, M. Chen, Y. Zhao, T. Tao, Z. Xu, G. Liu, Fabrication of a biomass-based hydrous zirconium oxide nanocomposite for preferable phosphate removal and recovery, ACS Appl. Mater. Interfaces 7 (2015) 20835–20844.

[48] B. Liu, W. Song, W. Zhang, X. Zhang, S. Pan, H. Wu, Y. Sun, Y. Xu, Fe3O4@CNT as a high-effective and steady chainmail catalyst for tetracycline degradation with

[49] peroxydisulfate activation: performance and mechanism, Sep. Purif. Technol. 273 (2021), 118705.

[49] J. Wang, S. Wang, Reactive species in advanced oxidation processes: Formation, identification and reaction mechanism, Chem. Eng. J. 401 (2020), 126158.

[50] L. Tang, Y. Liu, J. Wang, G. Zeng, Y. Deng, H. Dong, H. Feng, J. Wang, B. Peng, Enhanced activation process of persulfate by mesoporous carbon for degradation of aqueous organic pollutants: electron transfer mechanism, Appl. Catal. B Environ. 231 (2018) 1–10.

[51] E.-T. Yun, J.H. Lee, J. Kim, H.-D. Park, J. Lee, Identifying the nonradical mechanism in the peroxymonosulfate activation process: singlet oxygenation versus mediated electron transfer, Environ. Sci. Technol. 52 (2018) 7032–7042.

[52] Q. Yi, J. Ji, B. Shen, C. Dong, J. Liu, J. Zhang, M. Xing, Singlet oxygen triggered by superoxide radicals in a molybdenum cocatalytic fenton reaction with enhanced REDOX activity in the environment, Environ. Sci. Technol. 53 (2019) 9725–9733.

[53] Y. Gao, Y. Zhu, L. Lyu, Q. Zeng, X. Xing, C. Hu, Electronic structure modulation of graphitic carbon nitride by oxygen doping for enhanced catalytic degradation of organic pollutants through peroxymonosulfate activation, Environ. Sci. Technol. 52 (2018) 14371–14380.

[54] R.J. Martínez, J. Farrell, Understanding nitrilotris(methylenephosphonic acid) reactions with ferric hydroxide, Chemosphere 175 (2017) 490–496.

[55] Z.-H. Xie, C.-S. He, H.-Y. Zhou, L.-L. Li, Y. Liu, Y. Du, W. Liu, Y. Mu, B. Lai, Effects of molecular structure on organic contaminants' degradation efficiency and dominant ROS in the advanced oxidation process with multiple ROS, Environ. Sci. Technol. 56 (2022) 8784–8795.

[56] M. Al Hamad, S.A. Al-Sobhi, A.T. Onawole, I.A. Hussein, M. Khraisheh, Density-functional theory investigation of barite scale inhibition using phosphonate and carboxyl-based inhibitors, ACS Omega 5 (2020) 33323–33328.

[57] B. He, L. Song, Z. Zhao, W. Liu, Y. Zhou, J. Shang, X. Cheng, CuFe2O4/CuO magnetic nano-composite activates PMS to remove ciprofloxacin: ecotoxicity and DFT calculation, Chem. Eng. J. 446 (2022), 137183.

[58] S. Ma, D. Yang, Y. Guan, Y. Yang, Y. Zhu, Y. Zhang, J. Wu, L. Sheng, L. Liu, T. Yao, Maximally exploiting active sites on Yolk@shell nanoreactor: nearly 100% PMS activation efficiency and outstanding performance over full pH range in Fenton-like reaction, Appl. Catal. B Environ. 316 (2022) 121594.

[59] L. Cumbal, A.K. SenGupta, Arsenic removal using polymer-supported hydrated iron (III) oxide nanoparticles: role of donnan membrane effect, Environ. Sci. Technol. 39 (2005) 6508–6515.

[60] Y. Wang, C. Liu, Y. Zhang, W. Meng, B. Yu, S. Pu, D. Yuan, F. Qi, B. Xu, W. Chu, Sulfate radical-based photo-Fenton reaction derived by CuBi2O4 and its composites with α-Bi2O3 under visible light irradiation: catalyst fabrication, performance and reaction mechanism, Appl. Catal. B Environ. 235 (2018) 264–273.

[61] M. Li, B. Zhang, S. Zou, Q. Liu, M. Yang, Highly selective adsorption of vanadium (V) by nano-hydrous zirconium oxide-modified anion exchange resin, J. Hazard. Mater. 384 (2020), 121386.

[62] F.J. Rivas, Monopersulfate in water treatment: Kinetics, J. Hazard. Mater. 430 (2022), 128383.

[63] S. Khan, X. He, J.A. Khan, H.M. Khan, D.L. Boccelli, D.D. Dionysiou, Kinetics and mechanism of sulfate radical- and hydroxyl radical-induced degradation of highly chlorinated pesticide lindane in UV/peroxymonosulfate system, Chem. Eng. J. 318 (2017) 135–142.

[64] S. Yang, P. Wang, X. Yang, L. Shan, W. Zhang, X. Shao, R. Niu, Degradation efficiencies of azo dye Acid Orange 7 by the interaction of heat, UV and anions with common oxidants: persulfate, peroxymonosulfate and hydrogen peroxide, J. Hazard. Mater. 179 (2010) 552–558.

[65] J. Deng, S. Feng, K. Zhang, J. Li, H. Wang, T. Zhang, X. Ma, Heterogeneous activation of peroxymonosulfate using ordered mesoporous Co3O4 for the degradation of chloramphenicol at neutral pH, Chem. Eng. J. 308 (2017) 505–515.

[66] S. Yang, P. Wu, J. Liu, M. Chen, Z. Ahmed, N. Zhu, Efficient removal of bisphenol A by superoxide radical and singlet oxygen generated from peroxymonosulfate activated with Fe0-montmorillonite, Chem. Eng. J. 350 (2018) 484–495.

[67] Y. Wu, Y. Shi, H. Chen, J. Zhao, W. Dong, Activation of persulfate by magnetite: Implications for the degradation of low concentration sulfamethoxazole, Process Saf. Environ. Prot. 116 (2018) 468–476.

[68] Y. Pan, M. Zhou, Y. Zhang, J. Cai, B. Li, X. Sheng, Enhanced degradation of Rhodamine B by pre-magnetized Fe0/PS process: parameters optimization, mechanism and interferences of ions, Sep. Purif. Technol. 203 (2018) 66–74.

[69] C. Luo, J. Ma, J. Jiang, Y. Liu, Y. Song, Y. Yang, Y. Guan, D. Wu, Simulation and comparative study on the oxidation kinetics of atrazine by UV/H2O2, UV/HSO5− and UV/S2O82−, Water Res. 80 (2015) 99–108.

[70] J. Zhang, H. Song, Y. Liu, L. Wang, D. Li, C. Liu, M. Gong, Z. Zhang, T. Yang, J. Ma, Remarkable enhancement of a photochemical Fenton-like system (UV-A/Fe(II)/PMS) at near-neutral pH and low Fe(II)/peroxymonosulfate ratio by three alpha hydroxy acids: mechanisms and influencing factors, Sep. Purif. Technol. 224 (2019) 142–151.

[71] D. He, Z. Luo, X. Zeng, Q. Chen, Z. Zhao, W. Cao, J. Shu, M. Chen, Electrolytic manganese residue disposal based on basic burning raw material: Heavy metals solidification/stabilization and long-term stability, Sci. Total Environ. 825 (2022), 153774.

[72] T. Li, S. Lu, W. Lin, H. Ren, R. Zhou, Heat-activated persulfate oxidative degradation of ofloxacin: Kinetics, mechanisms, and toxicity assessment, Chem. Eng. J. 433 (2022), 133801.